THIRD ANNUAL PROGRESS REPORT

AN INVESTIGATION OF STRAIN CYCLING BEHAVIOR OF 7075-T6 ALUMINUM UNDER COMBINED STATE OF STRAIN

by

S. Y. Zamrik

Department of Engineering Mechanics
The Pennsylvania State University

Supported by

National Aeronautics and Space Administration
Research Grant NGR-39-009-034

University Park, Pennsylvania
October 1, 1967

THIRD ANNUAL PROGRESS REPORT

An Investigation of Strain Cycling Behavior of 7075-T6 Aluminum under Combined State of Strain

by

S. Y. Zamrik

Department of Engineering Mechanics
The Pennsylvania State University

Supported by

National Aeronautics and Space Administration
Research Grant NGR-39-009-034

[redacted]

University Park, Pennsylvania
October 1, 1967

Preface

This is the third annual progress report, covering the research work on anticlastic bending. A method to introduce a diversified biaxial strain ratio is discussed and the results are compared on the basis of three failure theories for low-cycle fatigue studes. The reported results are part of a research program on "Biaxial Strain Cycling Effect on Fatigue Life of Structural Materials," supported by the National Aeronautics and Space Administration under Research Grant NGR-39-009-034.

Acknowledgments

The assistance of Messrs. T. Goto, John Shewchuk and Koji Mizuhata in conducting the tests is gratefully acknowledged.

Abstract

The uniaxial and biaxial low cycle fatigue life of 7075-T651 aluminum alloy in anticlastic bending is investigated. Uniaxial data is obtained from a cantilever specimen and rhombic plate specimens are used for nominal strain biaxiality of 1:-1, 1:-0.9, 1:-0.8 and 1:-0.5. Experimental data is discussed on the basis of maximum strain range, maximum shear strain range and octahedral shear strain range.

Table of Contents

Table of Contents (continued)

Page

List of Figures

List of Figures (continued)

List of Figures (continued)

List of Tables

Nomenclature

e	strain
e_1, e_2, e_3	principal strains
Δe	strain range
Δe_E	elastic strain range
Δe_p	plastic strain range
Δe_1	maximum strain range
e_f	ductility
σ	stress
σ_1, σ_2, σ_3	principal stresses
$\Delta\sigma$	stress range
γ	shear strain
$\Delta\gamma_p$	plastic shear strain range
γ_{max}	maximum shear strain
$\Delta\gamma_{max}$	maximum shear strain range
γ_{oct}	octahedral shear strain
$\Delta\gamma_{oct}$	octahedral shear strain range
$\Delta\gamma_{op}$	plastic octahedral shear strain range
E	modulus of elasticity
η	second modulus
μ	Poisson's ratio
N	number of cycles to failure
a, b	diagonal lengths of rhombic specimen
ϕ	strain ratio $= e_2/e_1$
h	thickness of rhombic specimen

Nomenclature (continued)

M_x, M_y	bending moments per unit length directed along the reference axes
w	deflection
n	constant
C	constant

1. Introduction

The main objective of the research program is to conduct an experimental investigation on multiaxial strain cycling and to evolve a theory for predicting multiaxial strain behavior from a uniaxial strain cycling relation.

It appears from the studies conducted so far, that the octahedral shear strain is the controlling function describing strain cycling behavior for in-phase strain state conditions.

To achieve a diversified biaxial strain ratio, two low-cycle fatigue machines were designed and constructed. The first machine introduces combined axial and torsional strain cycling under in-phase or out-of-phase loading conditions, utilizing thin hollow cylindrical specimens. The second machine subjects anticlastic plate specimens to biaxial strain ratios under pure bending load.

This report covers the design of low-cycle anticlastic bending fatigue machines, anticlastic test specimens and the experimental results.

Test results, based on maximum strain range, maximum shear strain range and octahedral shear strain range theories are presented in a series of strain versus number of cycles to failure curves.

2. Application of Anticlastic Bending to Multiaxial Strain Cycling-Low-Cycle Fatigue

The use of reversed bending technique is not new in low-cycle fatigue studies under biaxial loading. Gross, Tsang and Stout (1,2,3,4) used a cantilever bending of wide specimens with a width-to-thickness ratio of five to simulate the biaxial stress state of 2:1 stress ratio which was encountered in pressure vessels. This stress condition is caused by a lateral constraint against free deformation along the center line of the specimens for an ideal plastic material of Poisson's ratio μ of 1/2.

Later Sachs, Weiss et al (5,6,7) at Syracuse University modified this technique to cover a wider stress ratio ranging from 1:0 to 2:1 (for ideal plastic material) by changing the width-to-thickness ratio of specimens, which resulted in a variation of degree of constraint of lateral deformation. The stress ratios, 1:0 to 2:1, produce the principal strain ratios of 2:-1 to 1:0 (for ideal plastic material).

Other methods producing biaxial stress condition on the surface of plate specimens, were developed by Blaser et al (8) and by Bowman and Dolan (9). This was achieved by pulsating pressure on one side of a rectangular specimen, simply supported along its edges. Ives et al (10) modified this method to attain completely reversed bending by subjecting a circular specimen, simply supported along its edge, to pressure alternately on one of two sides of specimen surface.

The foregoing method has been modified by Shewchuk and Zamrik (11) to cover a wider range of strain ratios from 1:1 to 2:1 by employing oval specimens with different diametral ratios.

With the use of anticlastic bending of rhombic plate specimens, a completely different range of strain ratios are covered, simply by changing the diagonal ratio of the rhombic plate specimens. Anticlastic bending of a rhombic plate is a case of pure bending of a plate having two principal curvatures of opposite signs (Figure 1). Therefore, the stress state on the specimen surface is biaxial tension-compression.

Figure 2 shows the covered area of stress and strain ratios by the above-mentioned three different methods: wide cantilever bending (5,6,7), pressurization of oval and circular plates and anticlastic bending. However, each of these methods has its own feature and may supplement each other.

One of the advantages of the anticlastic bending method is in the uniform distributions of stress and strain over the specimen surface. This is simply achieved if one considers the rhombic plate to constitute beams of uniform strength along its two diagonals where the simple beam theory (12) can be used as a first approximation. In the wide-cantilever bending method, the segment subjected to the maximum stress or strain state is limited to a small area on the specimen surface. The oval plate under pressurization, has, also a limited area which is around the center of the plate, when subjected to the maximum stress or strain state.

In the reversed bending experiments, a low-value of thickness-to-representative-length ratio of bending specimens is usually employed. In this case, a large deflection of bending specimens is needed to attain a large strain amplitude. This is usually hindered by limitations due to geometrical configurations of both the bending specimens and the testing fixtures used. With the use of large value of thickness-to-representative-length ratio of the bending specimens, the large deflection limitation can be eliminated. However, this often causes a large shearing force for bending, which may introduce a large

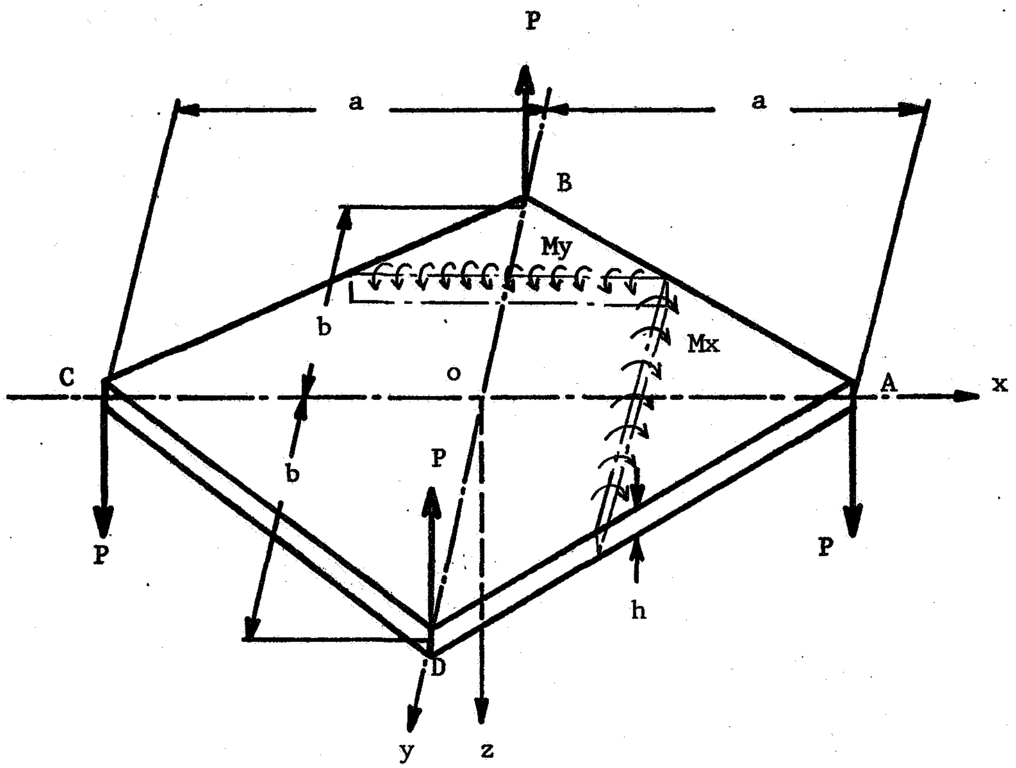

Figure 1. Rhombic Plate Under Anticlastic Bending

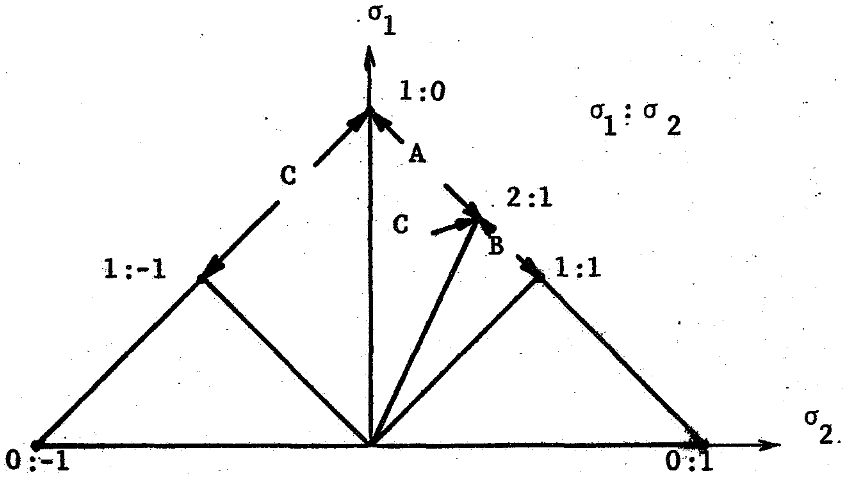

Figure 2A. Stress Ratios Covered by

(A) Wide-Cantilever Bending (5,6,7)

(B) Pressurization of Oval Plate (11)

(C) Anticlastic Bending

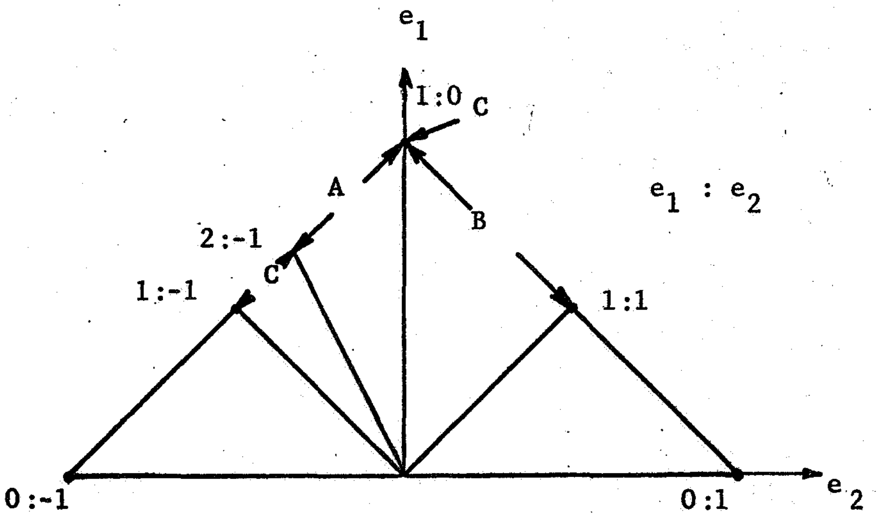

Figure 2B. Strain Ratios Covered by

(A) Wide-Cantilever Bending (5,6,7)

(B) Pressurization of Oval Plate (11)

(C) Anticlastic Bending

shear stress and strain on the neutral plane of the bending specimens, resulting in premature failure along this plane. This difficulty can be avoided with the use of anticlastic plate specimens where several percents of strain amplitude can be imposed without premature shear fracture along the neutral plane.

In summary, the anticlastic bending method for investigating biaxial strain-cycling low-cycle fatigue properties of materials has the following characteristics:

(1) Uniform distribution of stress and strain over the entire specimen surface,

(2) possibility of preventing generation of mean stress and strain in specimen,

(3) the special covered regions of stress and strain state, which are the same as in the case of the combined push-pull axial and torsion load, and

(4) occurrence of little error in computing e_3 due to use of inaccurate value of μ.

Cases (3) and (4) are discussed in Section 12 with special reference to the strain state.

3. Design and Construction of the Anticlastic Bending Low-Cycle Fatigue Testing Machine

The testing machine was designed and constructed to investigate the multiaxial low-cycle fatigue under constant deflection cycling. The extreme value of the stress ratio 1:0 is difficult to produce experimentally by anticlastic bending of rhombic specimens. This extreme state can be theoretically produced by lengthening one of the diagonals satisfactorily. Therefore, simple bending of a cantilever specimen, with the critical section of the same width as the thickness, was employed. This gives a stress ratio of 1:0 and produces a strain ratio of 1:-0.5 on the surface at the critical section.

The testing machine (Figure C-1 - Appendix C) is composed of four major parts, a loading system, a hydraulic power supply, a deflection monitor, and a frame. A schematic flow chart relating these parts is shown in Figure C-2.

4. Loading Mechanism for Anticlastic Bending of the Rhombic Specimen

The loading mechanism is illustrated in Figure C-3. It was designed to simply-support the rhombic specimen and to apply cyclic loading. The rhombic specimens are shown in Figure C-4 and the cantilever bending specimen in Figure C-5. Ideal anticlastic bending of a rhombic plate is conducted by applying concentrated forces at the four corners of the plate in the direction of the thickness (Figure 1). However, rollers through which the applied forces act on the specimen were used to avoid mean strain effect and unnecessary stress concentrations. Specimen with rollers was mounted in two pair of holders. Each holder was attached to the respective die set by a pair of connectors.

The loading mechanism has the capacity to hold a specimen whose shorter diagonal length is between two and three inches and whose longer diagonal length is from two to four inches, and of subjecting the specimen to a deflection amplitude of about ± 1.0 inch.

5. Loading Mechanism for Cantilever Bending

The assembly of this mechanism is illustrated in Figure C-6. The cantilever specimens shown in Figure C-5 were subjected to cyclic loading in the same way as the rhombic specimens. Load was applied to the specimen through the same roller that was used for the rhombic specimens.

The loading mechanism subjected the specimen to cyclic deflection of about ±1 inch.

6. Hydraulic System

A hydraulic system was used as a power supply. This system (schematically illustrated in Figure C-7) has a linear actuator connected with the upper part of the die set, and a four-way flow-control valve. The travelling speed of the hydraulic ram of the linear actuator was controlled by adjusting the throttle valve six and the bypass valve five. The travelling direction and the stop of the ram were controlled by switches A and B in the solenoid circuit including the four-way valve.

The electrical circuit shown schematically in Figure C-8 consists of a counter to record the number of loading cycles and a microswitch C. The switch C was fixed in the deflection monitor and operated by it. The travel of the ram was automatically controlled in the way of cyclic deflection by switch C and the deflection monitor.

7. Deflection Monitor

The fatigue tests were conducted at various deflection amplitudes. To control and keep the deflection amplitude constant, a deflection monitor was devised. The deflection monitor consisted of a follower, a scaled disc and a microswitch C as shown in Figure C-9. The follower moves in coincidence with the hydraulic ram of the linear actuator. This movement is converted to a rotation of the disc by a rack and pinion. On the disc two adjustable stops A and B are attached and they contact the plate spring of the microswitch C at any displacement of the hydraulic ram. Also on the disc, the deflection scale was marked in 0.05 inch divisions with a total range of ±0.75 inch. The indicating scale was directly marked by observing the follower travel in increments of 0.05 inch by a dial indicator. To assure constancy of the deflection amplitude during tests, a dial indicator was fixed to the die set.

8. Frame

To hold the loading mechanism and the linear actuator in the vertical line, a frame, shown in Figure C-10 was constructed.

9. Experimental Procedure

A. Calibration Tests

Calibration tests were carried out for the following purposes: (1) to check the uniformity of strain state over the entire surface of the rhombic specimens under deflection, and (2) to obtain a relation between deflection and corresponding strain state on the surface of each type of specimen.

Before the calibration tests were conducted, two specimens were arbitrarily chosen from each series of specimens. Their widths and thicknesses were measured to determine the variation in these dimensions. These were less than the order of 0.01 inch.

From this selection, BLH SR-4 PA-7 strain gages were cemented on the surface of the rhombic and the cantilever specimens at locations indicated in Figure A-1 (Appendix A). Before the specimen was placed between the die set, the hydraulic ram was brought to the null-position. The null-position occurs when the faces of the upper and base die set are 4.5 inches apart. The deflection scale position was brought to the zero position with the help of the adjustable screw. First, the upper pair of holders were adjusted symmetrically about the die center, so that the distance between their faces was 1/4 inch less than the shorter diagonal of the specimen. The specimen was then placed in the holders and the shelter plates were fixed. The lower pair of holders were aligned with the longer diagonal of the specimen. Finally, the specimen was adjusted in position, and shelter plates of the lower holders were fixed.

The calibration results are shown as strains versus deflection curves in Figures B-1, B-2, B-3 and B-4 (Appendix B). Figures B-5, B-6, B-7 and B-8 show the relations between maximum strain range, strain ratio and deflection amplitude for each series of the specimens.

Deflection test results show:

(1) Uniformity of strain state over the surfaces can be maintained under any deflection.

(2) The relation between strain range and deflection is linear under deflection amplitude of more than 0.1 inch.

(3) The variation in the slopes of the calibration curves for the early part of the deflection amplitude is due to the clearance between the roller and the holder.

10. Materials and Specimens

The material used in this study was 7075-T651 aluminum alloy rolled plate with a nominal thickness of 0.250 inch. The chemical composition and the mechanical properties of the material are given in Tables 1-A and 1-B, respectively. The cantilever specimens were cut from the as-received plates of configuration shown in Figure A-1-D (Appendix A). The rolling direction for the rhombic specimens was 45 degrees to the diagonals, and 45 degrees to the longitudinal direction for the cantilever specimens. Specimen surface was not polished.

After machining, the rhombic specimens were rounded along the edges with sandpaper of Emery number 00 to avoid crack initiations due to stress concentrations. Extreme precautions were taken in rounding the edges into approximately 1/16 inch radius without producing marks on the specimen surfaces, since stress concentrations at the corners were found to be significant. Materials with remarkable surface irregularities due to fabrication or handling were rejected.

11. Experimental Results

To supplement the existing biaxial strain data, strain ratios of 1:-1, 1:-0.9 and 1:-0.8 were chosen for the rhombic plate tests. Three series of rhombic plate specimens having the following diagonal lengths: three by three inches, two by two and a half inches and two by three inches, provided the selected strain ratios respectively. A strain state 1:-0.5 was obtained by the simple cantilever bending. By controlling constant deflection amplitude, fatigue tests were conducted

Table 1-A. Chemical Composition of 7075-T651 Aluminum Alloy

Chemical Composition	%
Cu	1.2
Mg	2.1
Mn	0.3
Fe	0.7
Si	0.5
Zn	5.1
Cr	0.2
Ti	0.2
Al	Remainder

Table 1-B. Mechanical Properties of 7075-T651 Aluminum Alloy

Yield Stress (0.2 percent strain)	69	ksi
Ultimate Stress	79	ksi
Ductility (2 inches gage length)	8	%
Modulus of Elasticity	10.3×10^3	ksi
Poisson's Ratio	.321	

in a cyclic life range between 60 and 1400 cycles. Failure was defined as the initiation of the first visible crack on the surface of the specimen.

The data of the anticlastic bending low-cycle fatigue tests are presented in tabular, and graphical forms with the data obtained from the cantilever bending tests. Test results of 57 from total 60 tests are reported.

Tables 2 through 6 (Appendix A) show the test results for each series of the 3x3, 2x2.5, and 2x3 inches rhombic specimens and the cantilever specimens. The values of the maximum strain range Δe_1 and the strain ratio ϕ were read directly from the calibration curves at each deflection amplitude.

Figures 3 through 6 show the log-log plots of the experimental results in terms of the maximum strain range Δe_1, the maximum shear strain range $\Delta\gamma_{max}$ and the octahedral shear strain range $\Delta\gamma_{oct}$ versus the number of cycles to failure N for each series of specimens. The maximum shear strain range $\Delta\gamma_{max}$ was calculated by the following equation:

$$\Delta\gamma_{max} = (1 - \phi)\Delta e_1/2 \tag{1}$$

where Δe_1 is the maximum principal strain range and $e_2 = \phi e_1$ is the minimum principal strain in the case of anticlastic bending. The octahedral shear strain range is expressed as:

$$\Delta\gamma_{oct} = \frac{2}{3}\left[(\Delta e_1-\Delta e_2)^2 + (\Delta e_2-\Delta e_3)^2 + (\Delta e_3-\Delta e_1)^2\right]^{1/2} \tag{2}$$

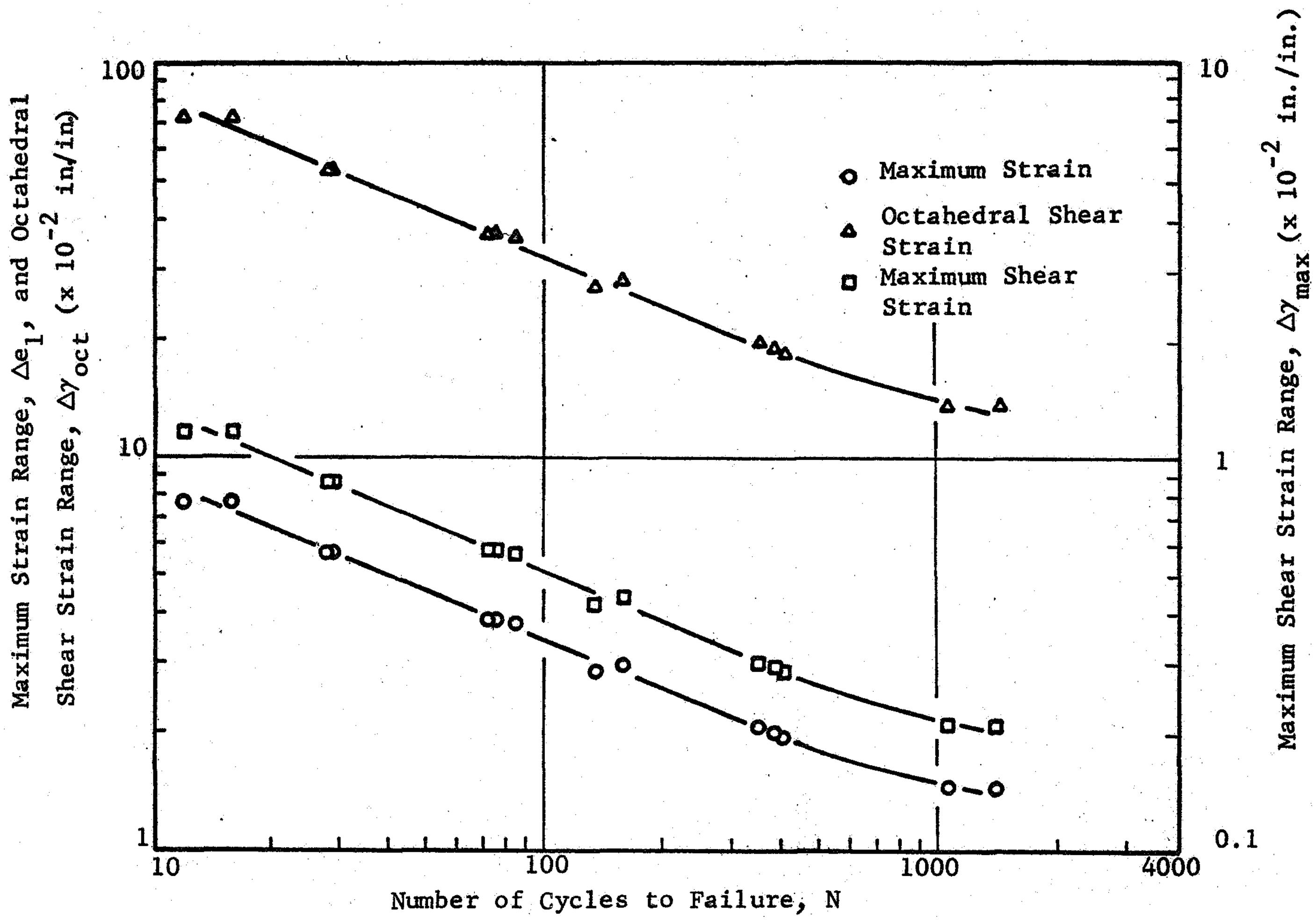

Figure 3. Maximum Strain Range, Maximum Shear Strain Range and Octahedral Shear Strain Range vs. Cycles to Failure for 2x2.5 Specimens

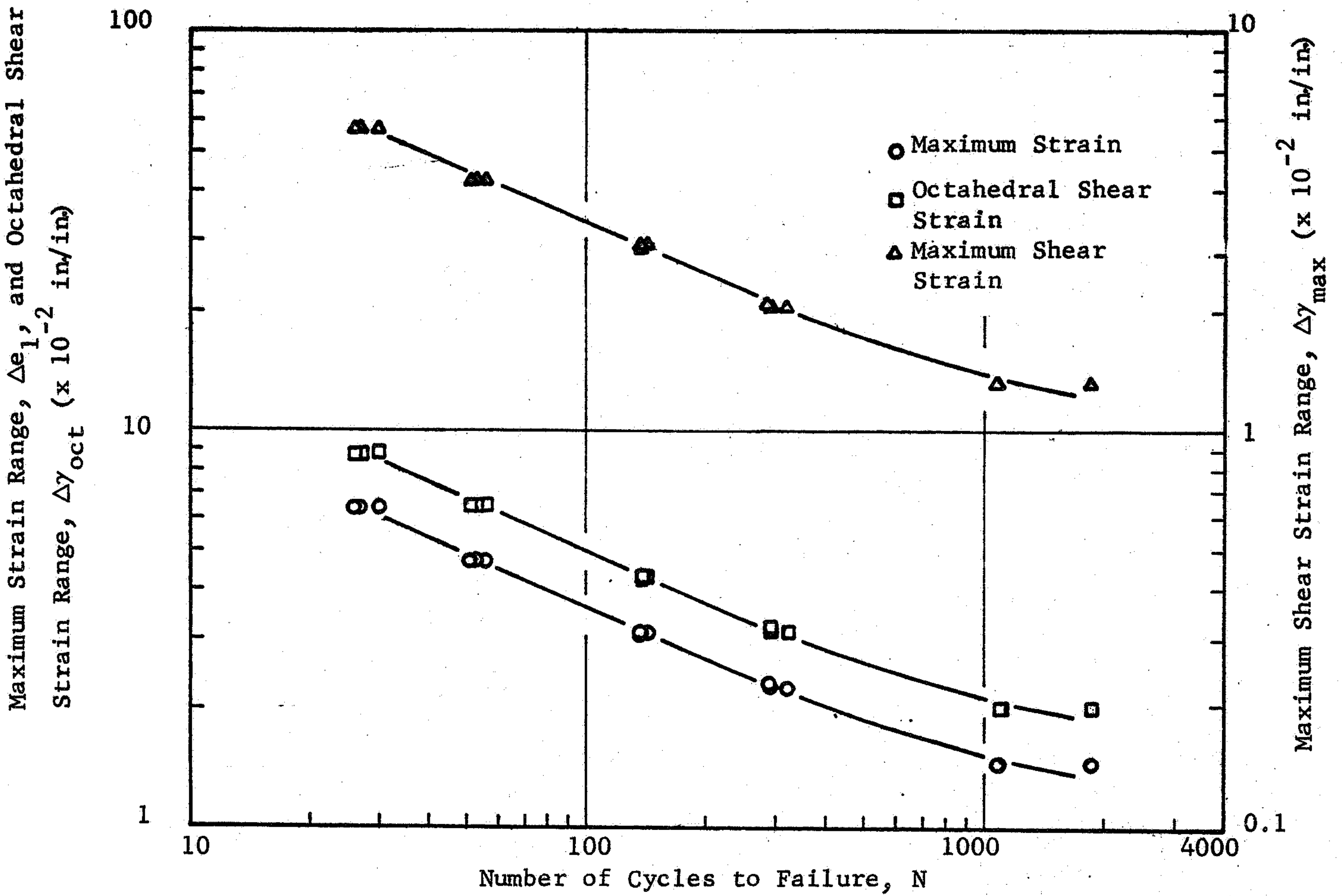

Figure 4. Maximum Strain Range, Maximum Shear Strain Range and Octahedral Shear Strain Range vs. Cycles to Failure for 2x3 Specimens

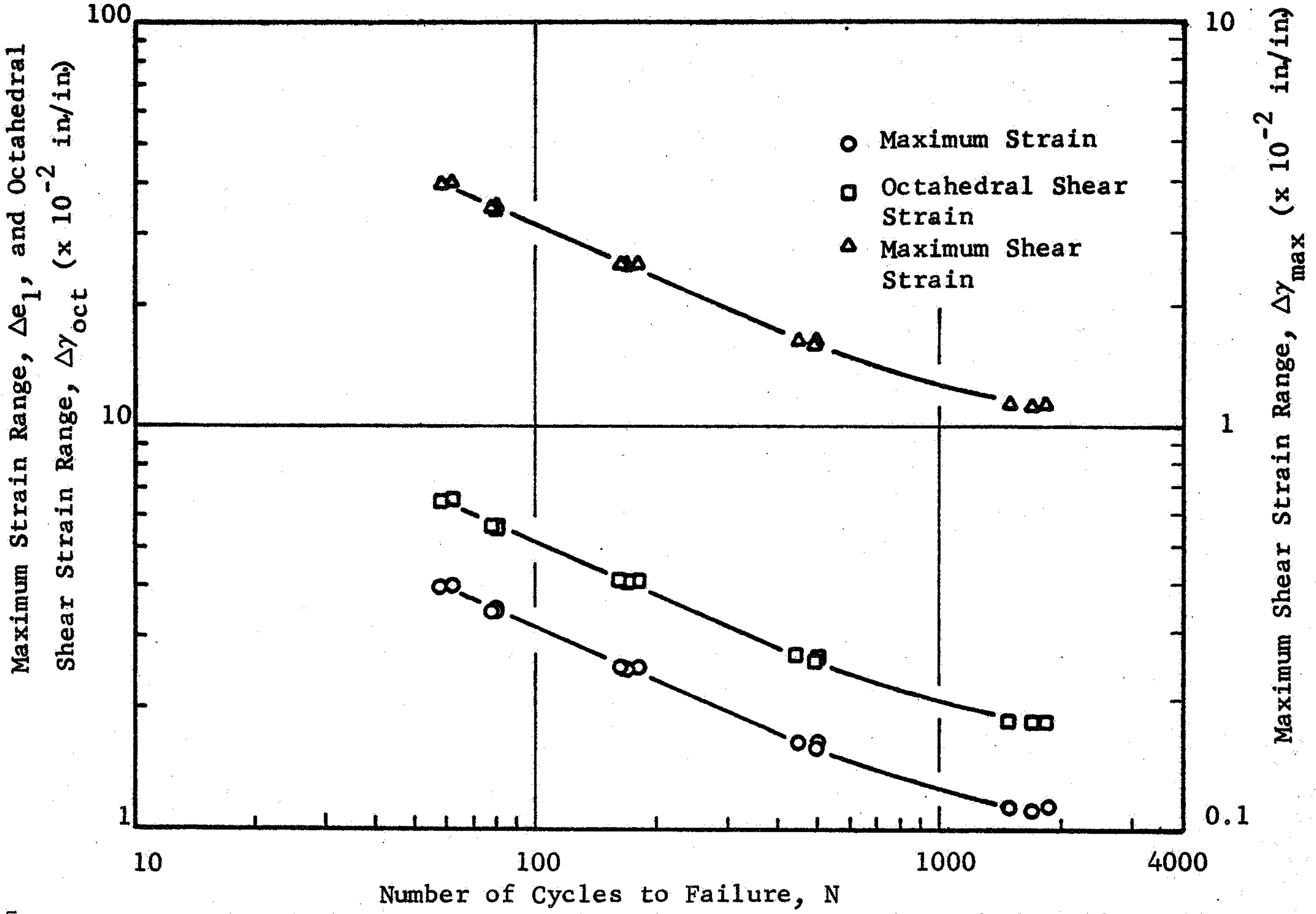

Figure 5. Maximum Strain Range, Maximum Shear Strain Range and Octahedral Shear Strain Range vs. Cycles to Failure for 3x3 Specimens

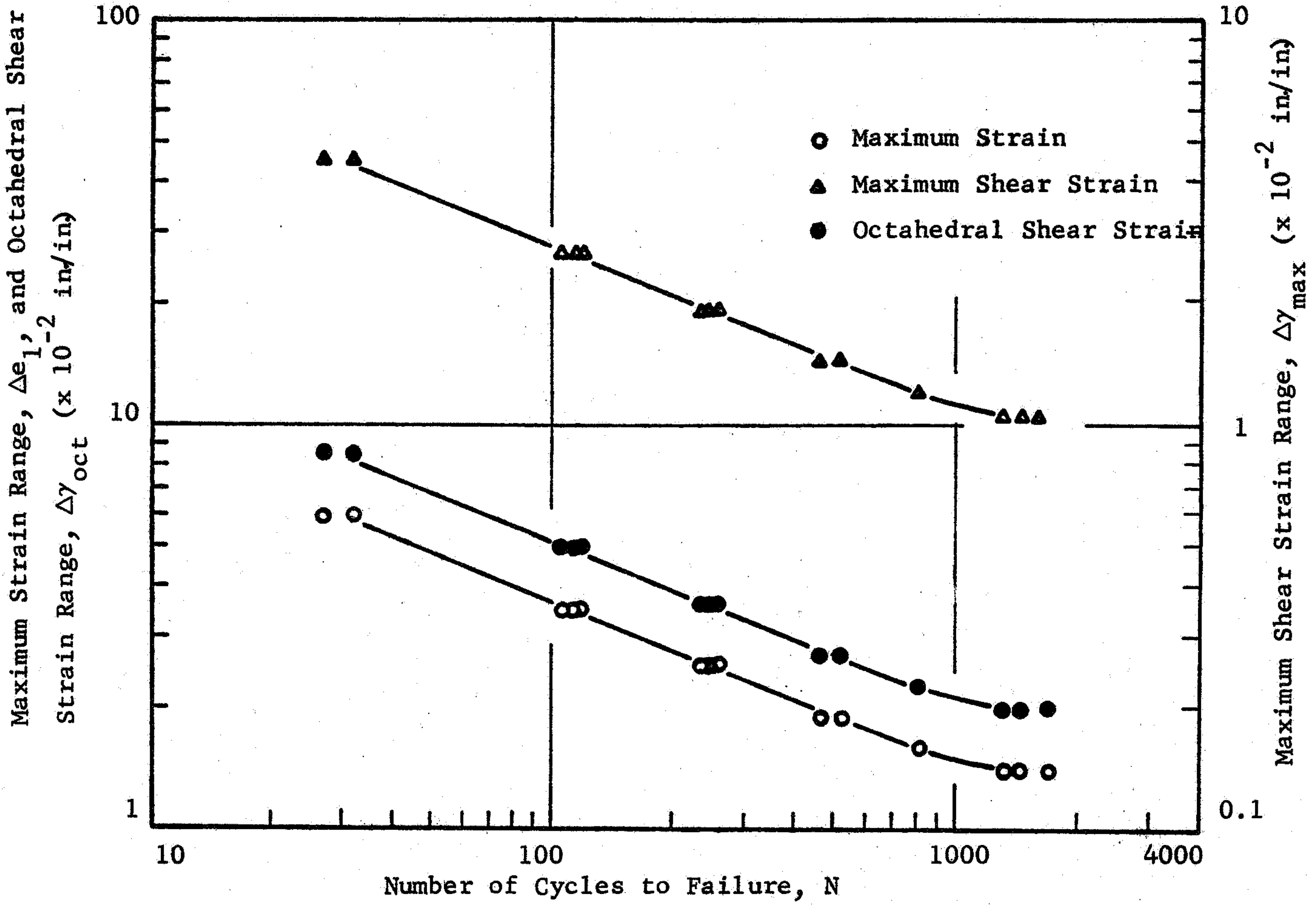

Figure 6. Maximum Strain Range, Maximum Shear Strain Range and Octahedral Shear Strain Range vs. Cycles to Failure for Cantilever Specimens

With the assumption of volume constancy, equation (2) changes to

$$\Delta\gamma_{oct} = 1.63(\phi^2 + \phi + 1)\Delta e_1 \tag{3}$$

for the case of biaxial stress state.

For the cantilever bending case, the maximum shear strain range $\Delta\gamma_{max}$ and the octahedral shear strain range $\Delta\gamma_{oct}$ values were calculated from:

$$\Delta\gamma_{max} = 0.75\ \Delta e \tag{4}$$

and

$$\Delta\gamma_{oct} = 1.41\ \Delta e \tag{5}$$

where Δe is the longitudinal strain range.

12. Octahedral Shear Strain Theory and Effect of Poisson's Ratio

Theoretical and experimental studies in high cycle fatigue have shown that failure under multiaxial stress condition can be represented by the octahedral shear stress theory. However, in low-cycle fatigue where the use of strain is more meaningful than stress, the octahedral shear stress theory can be rewritten in terms of strains. Accordingly, fatigue failure occurs when the maximum octahedral shear strain under fluctuating multiaxial loading is equal to the maximum octahedral shear strain under fluctuating uniaxial loading. This basic definition is expressed as:

$$\gamma_{oct} = \frac{2}{3}\left[(e_1-e_2)^2 + (e_2-e_3)^2 + (e_3-e_1)^2\right]^{1/2} \tag{6}$$

The octahedral shear strain again consists of two strains, namely elastic and plastic. However, if the plastic strain is predominant, then the elastic strain can be neglected. In such case, a general relation of the octahedral shear plastic strain range can be expressed in terms of number of cycles to failure as:

$$\Delta\gamma_{OP}N^{n} = C \tag{7}$$

where n and C are constants.

Equation (7) is equivalent to Manson's (13) proposed equation:

$$\Delta\varepsilon_{p}N^{n_0} = C_1 \tag{7a}$$

for the case of uniaxial strain cycling with zero mean strain.

Based upon equation (7), the multiaxial strain experimental results show a fatigue curve with characteristics similar to the uniaxial fatigue curve (Figure 7) suggested by Manson (14). However, when the total octahedral shear strain is plotted against the number of cycles to failure the familiar non-linearity of the fatigue curve versus the number of cycles is observed.

The reported results in this report are based on the total octahedral shear strain, rather than on the plastic component.

In anticlastic bending tests, two principal strains were measured on the surface of the specimen (biaxial strain cycling tests) and the third principal strain was calculated since it was not possible to obtain it quantitatively.

For an extreme plastic strain condition, constant volume condition yields:

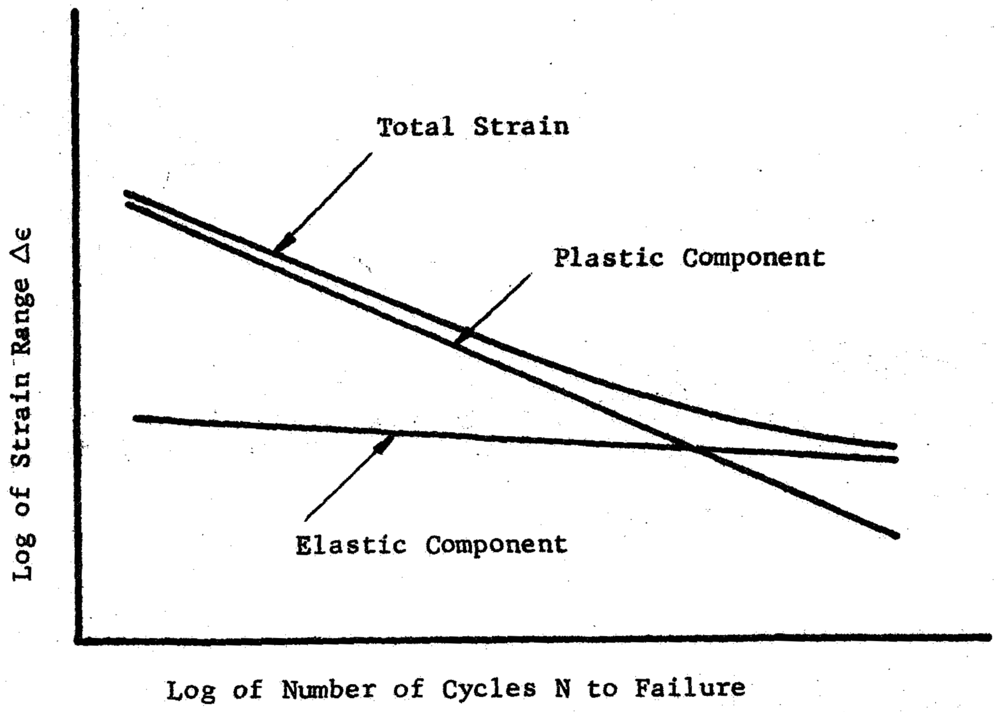

Figure 7. Fatigue Curve Suggested by Manson (14).

$$e_1 + e_2 + e_3 = 0 \tag{8}$$

The third principal strain e_3 is related to e_1, e_2 and μ by:

$$e_3 = - \frac{\mu}{1 - \mu} (e_1 + e_2) \tag{9}$$

for constant volume condition, $\mu = 0.5$.

However, it was found that Poisson's ratio μ has an effect on the octahedral shear strain. This effect is further explained in the following discussion.

By substituting the value of e_3 from equation (9) into equation (6) and using the strain ratio $\phi = e_2/e_1$ where e_1 is the maximum strain, a new expression for the octahedral shear strain for a biaxial strain condition is obtained as:

$$\gamma_{oct} = \frac{2\sqrt{2}}{3} \frac{1}{(1-\mu)} \left[(1-\mu+\mu^2)(1+\phi^2) - (1-4\mu+\mu^2)\phi \right]^{1/2} e_1 \tag{10}$$

where ϕ lies between -1 and +1, and μ between 0.3 and 0.5 depending on the strain state.

If γ_{oct}/e_1 is plotted against the strain ratio ϕ, with μ as a parameter, a family of curves is obtained as shown in Figure 8. Interchanging the parameter μ with ϕ, the family of curves are replotted in Figure 9. This family of curves reveals two interesting but related observations for the same value of e_1:

(1) The ratio of γ_{oct} at $\phi = 1$ (equibiaxial strain state) to that at $\phi = - \mu$ (uniaxial strain state) increases as μ increases and the ratio of γ_{oct} at $\phi = - 1$ (pure torsion strain state) to that at $\phi = -\mu$, decreases as μ increases, e.g.,

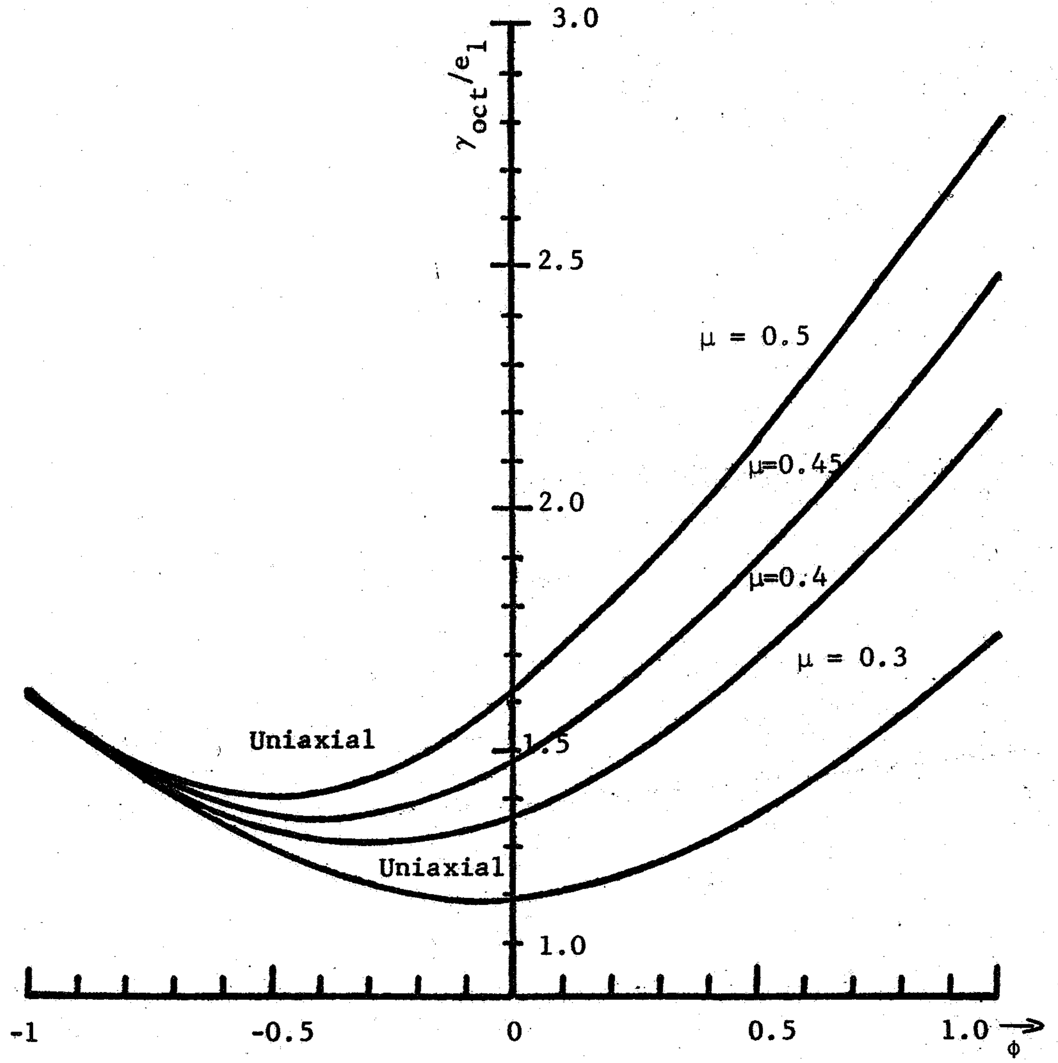

Figure 8. Octahedral Shear Strain vs. Strain Ratio at Constant Maximum Strain

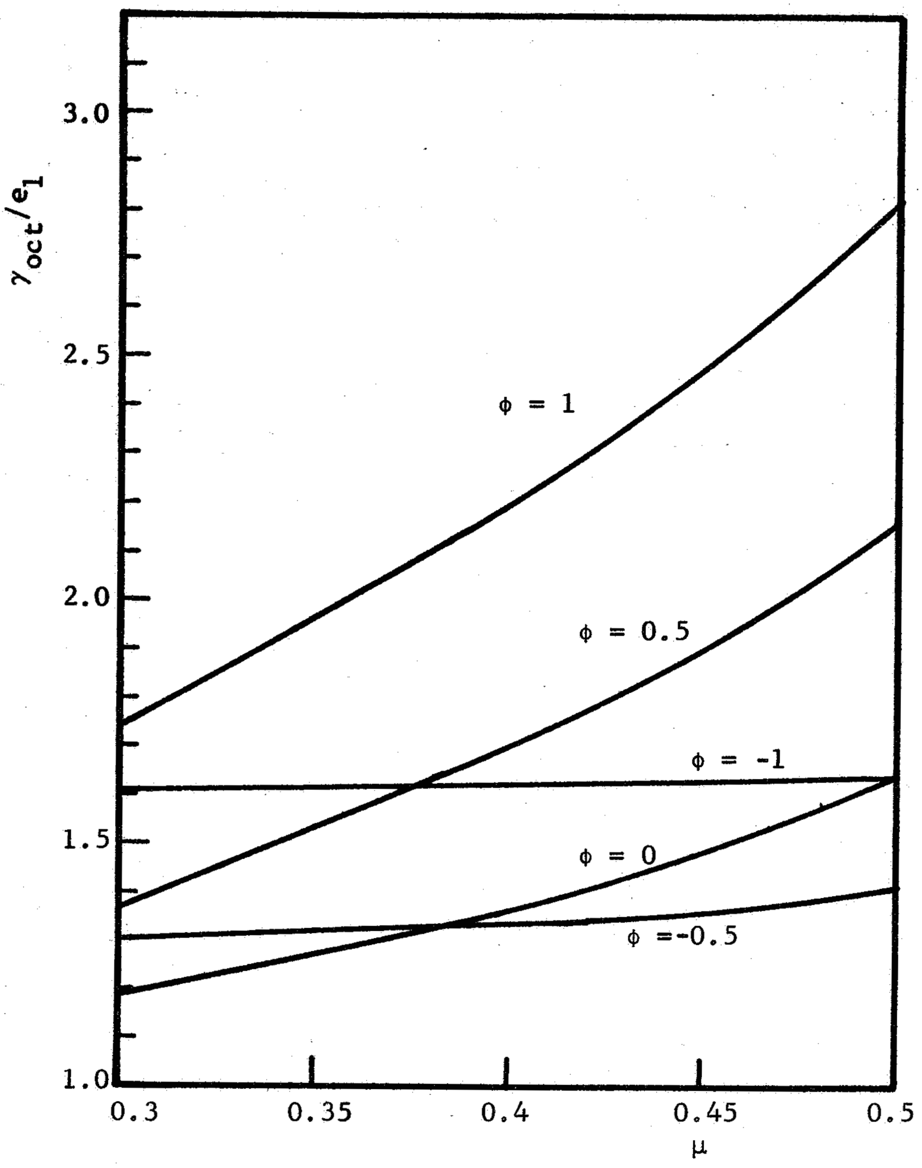

Figure 9. Octahedral Shear Strain vs. Poisson's Ratio at Constant Maximum Strain

		at $\mu=0.3$	at $\mu=0.4$	at $\mu=0.5$
$\frac{(\gamma_{oct})_{at\ \phi=1}}{(\gamma_{oct})_{at\ \phi=-\mu}}$	=	1.44	1.67	2.00
$\frac{(\gamma_{oct})_{at\ \phi=-1}}{(\gamma_{oct})_{at\ \phi=-\mu}}$	=	1.32	1.23	1.16

(2) As the value of ϕ changes from -1 to +1, the ratio of γ_{oct} at $\mu=0.5$ to γ_{oct} at a smaller value of μ increases and the tendency of the increment is significant for larger than -0.5, e.g.

		$\phi=-1$	$\phi=-0.5$	$\phi=0$	$\phi=1$
$\frac{(\gamma_{oct})_{at\ \mu=0.5}}{(\gamma_{oct})_{at\ \mu=0.3}}$	=	1.01	1.06	1.38	1.62
$\frac{(\gamma_{oct})_{at\ \mu=0.5}}{(\gamma_{oct})_{at\ \mu=0.45}}$	=	1.01	1.03	1.11	1.14

The two observations can be stated as: (1) the biaxial strain state has a pronounced effect on the value of γ_{oct} when $\phi = 1$ and less effect on the torsional side as the strain state is raised to extremely plastic, and, (2) the effect of Poisson's ratio on the value of γ_{oct} becomes significant when the biaxial strain state is between plane strain ($\phi=0$) and equibiaxial strain ($\phi=1$). It is interesting to note that the anticlastic bending and the combined push-pull and torsion tests are dealing with a strain state of strain ratio varying from 1:-1 to 1:-μ where the octahedral shear strain range changes from a maximum value (at $\phi=-1$) to a minimum value (at $\phi=-\mu$).

The error in γ_{oct} due to the use of inaccurate value of μ may be minimum for values around $\phi=-1$ and maximum for those near $\phi=+1$. Whether these errors should be taken into account depends on the accuracy of the measured variables in the test and on the significant digits to be presented for the results. The low-cycle fatigue data is usually presented in log-log plot of the strain range versus the number of cycles to failure, and significant number of digits of the strain range is usually two and the permissible range of strain is less than five percent. This means that an error of the order of one percent can be neglected; however if the strain state of ϕ is larger than zero, then the assumption of volume-constancy, if the true value of μ is less than 0.45, will lead to error that can not be neglected. Therefore a modified analysis of the octahedral shear strain theory is needed to account for the changes of μ.

13. Discussion

The test results show that the octahedral shear strain theory can be used as a good failure theory for multiaxial strain low-cycle fatigue. This can be seen if Figures 3 through 6 were replotted as Figures 10, 11 and 12.

To check the validity of this theory several available biaxial data which had not been interpreted from the point of view of the octahedral shear strain theory, were plotted for comparison purposes. For example, the biaxial strain-cycling data given by Sachs and Weiss, et al were replotted in terms of the octahedral shear strain range by using both the transverse to longitudinal strain ratio (7) and the

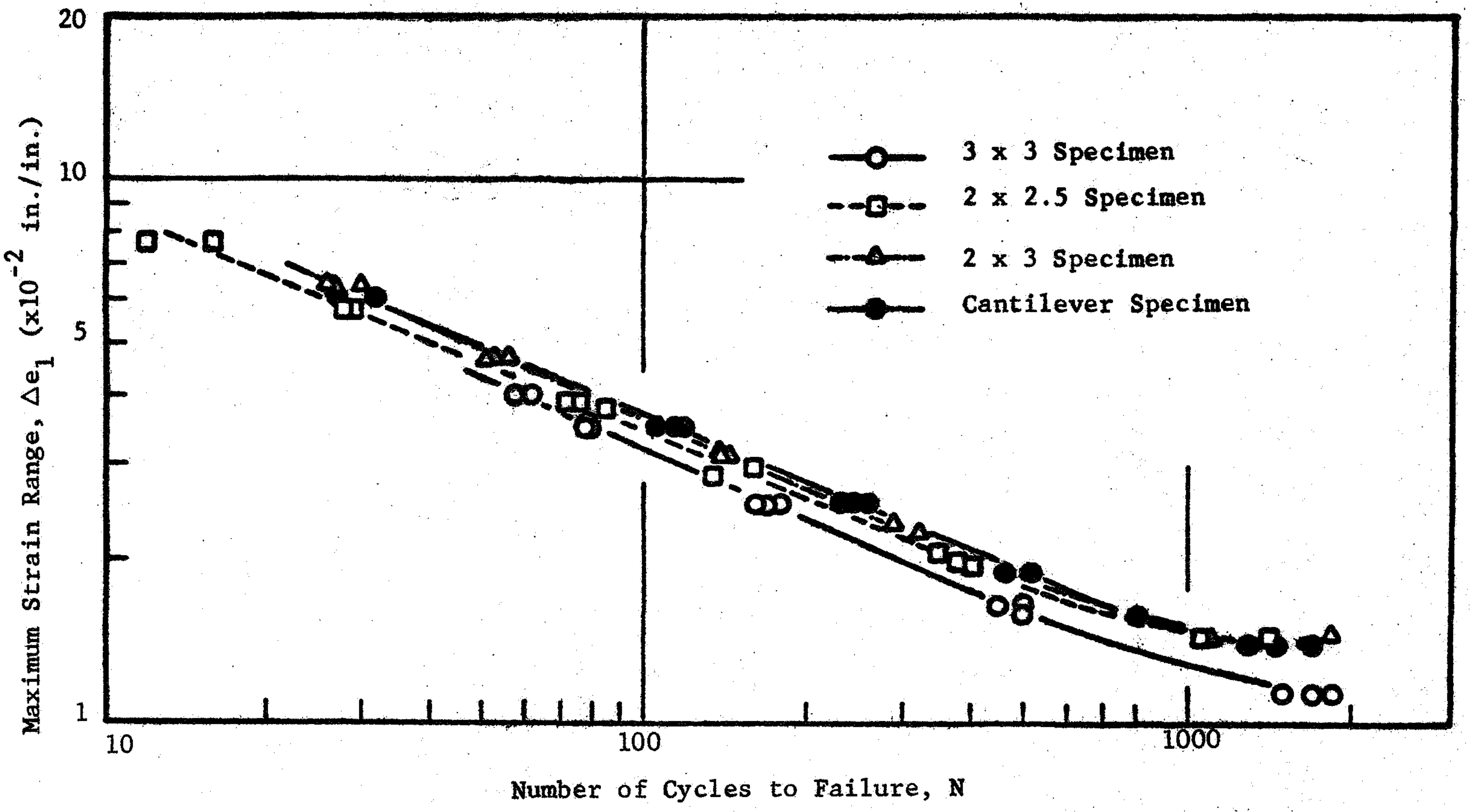

Figure 10. Comparison of Low-Cycle Fatigue Data Based on Maximum Strain Range

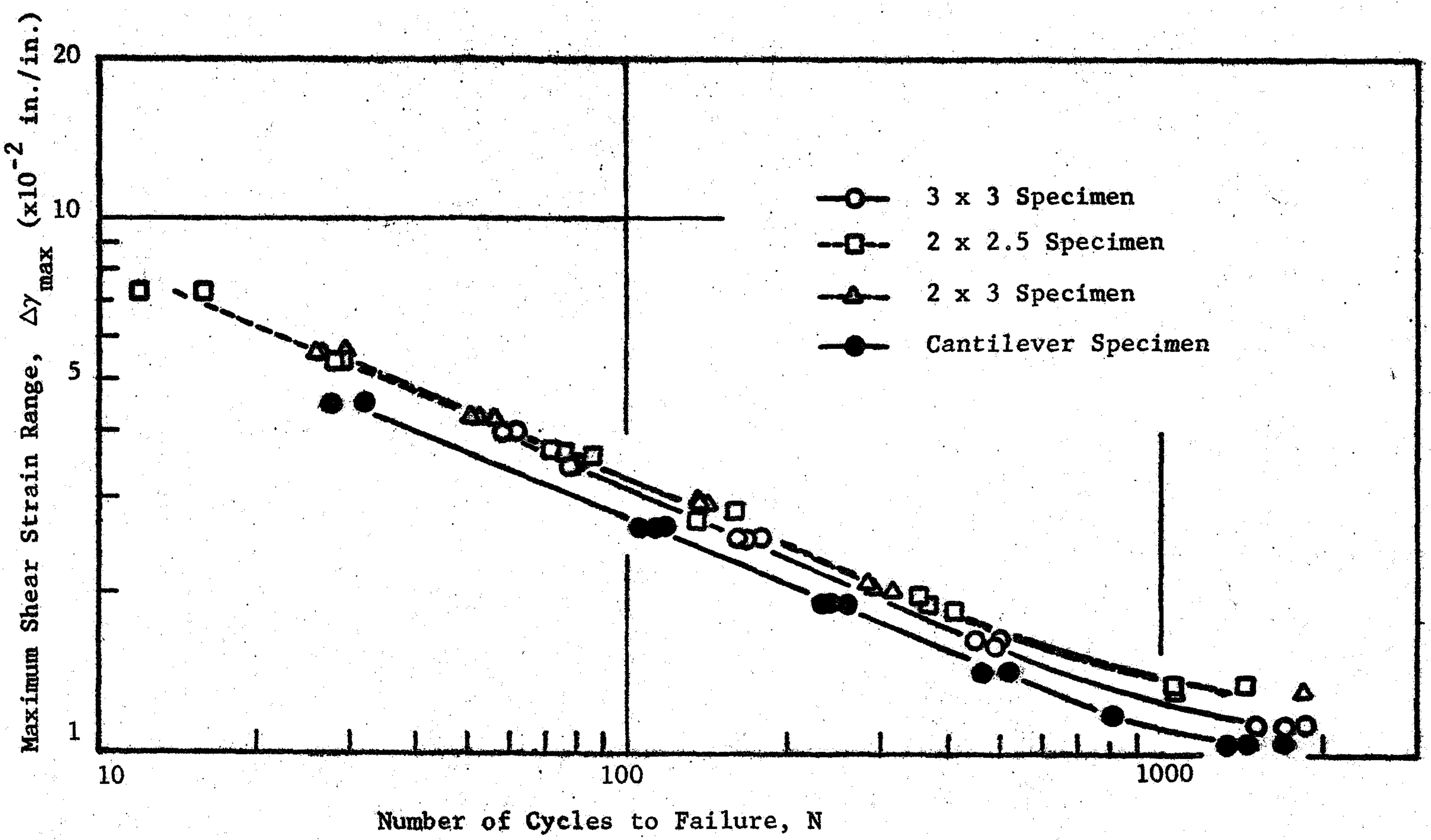

Figure 11. Comparison of Low-Cycle Fatigue Data Based on Maximum Shear Strain Range

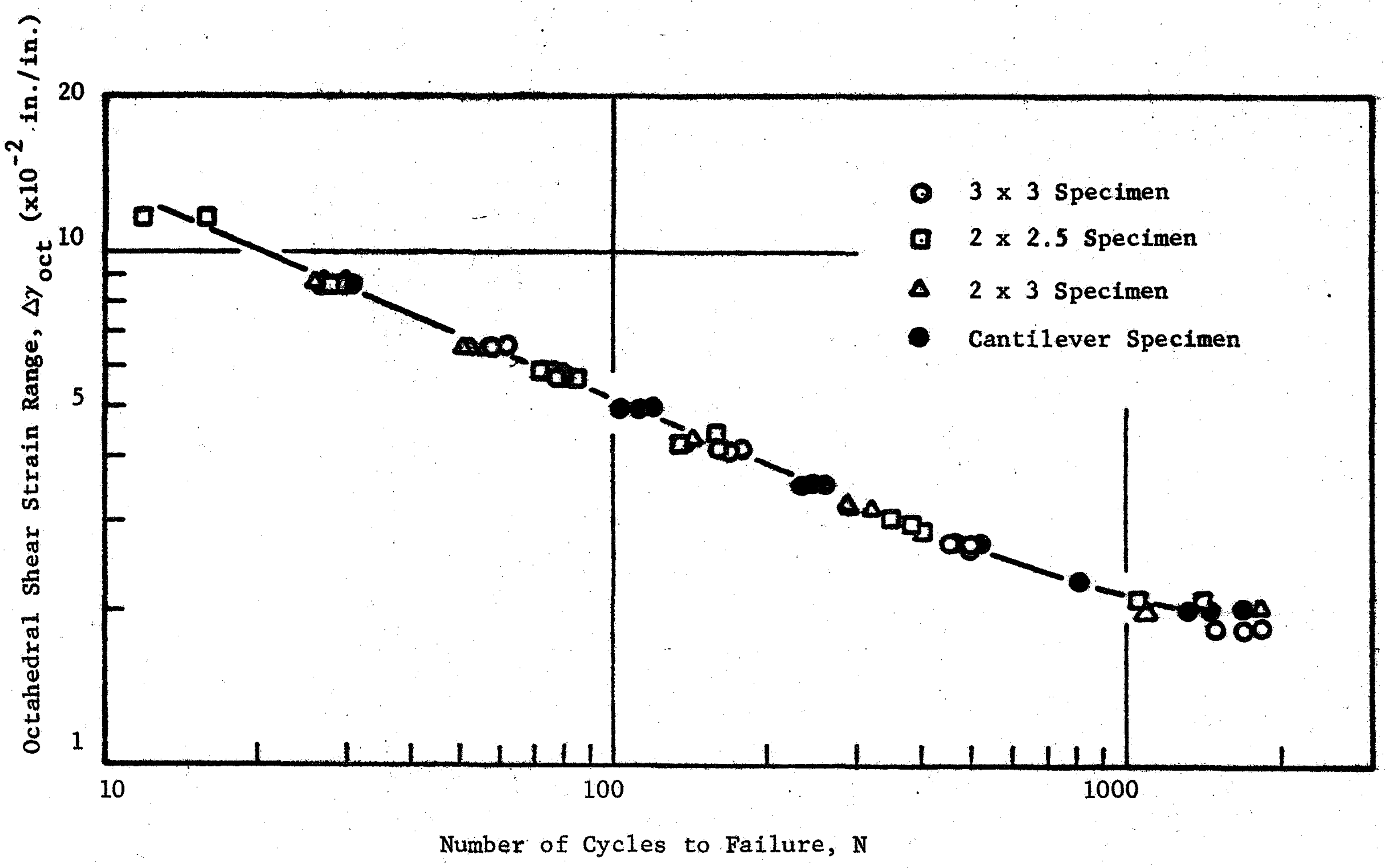

Figure 12. Comparison of Low-Cycle Fatigue Data Based on Octahedral Shear Strain Range

condition of volume-constancy. As shown in Figures 13, 14 and 15, a good simple curve of the results was obtained for the various strain ratios. The materials used in Sachs and Weiss' investigation were 5454-0 aluminum alloy, A-302 steel and 2024-T4 aluminum alloy. However a good agreement was not possible in the case of torsional loading. The torsional data presented by Halford and Morrow (15) on annealed 1100-0 aluminum was compared with the axial strain-cycling data reported on the same material by Manson and Hirshberg (14) and Tavernelli and Coffin (16). The result of the three reported data is shown in Figure 16. The agreement is not good and the torsion-test values were considerably greater than the axial test values. Again, data presented by Halford and Morrow on 7075-T5 aluminum alloy and SAE-4340 steel were compared with the axial strain-cycling data reported by Manson and Hirshberg. These results are shown in Figures 17 and 18. The possible difference in material properties and the difference in the definition of failure between the torsional and axial strain-cyclings could be the attributed factor for this scatter and lack of agreement.

Examples of surface failure are shown in Figures 19, 20 and 21 where a number of short cracks appeared on the 2x2.5 specimen surface when specimen was subjected to 0.199 percent maximum strain range cycling at 450 cycles; however, a long crack appeared on the surface of 3x3 specimens when subjected to 0.35 percent maximum strain range cycling at 82 cycles. Figure 22 shows the failure of cantilever specimen. Cracks can be seen not only in the direction of the rolling but also in the direction normal to the rolling direction. Such directions are coincident with the directions of the maximum shear and the octahedral shear on the specimen surfaces.

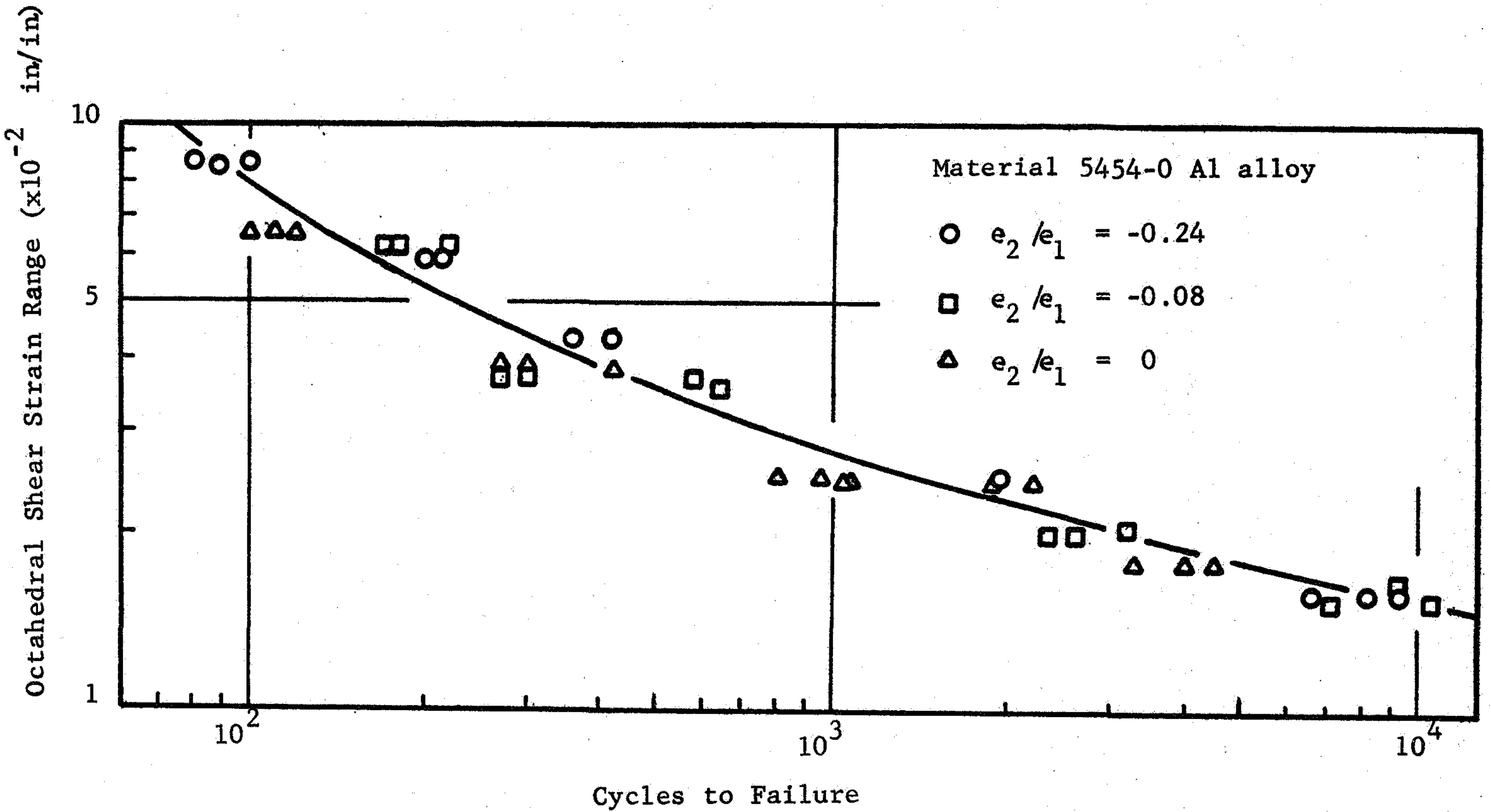

Figure 13. Comparison of Low-Cycle Fatigue Data Obtained Under Different Strain Multiaxialities Based on Octahedral Shear Strain for 5454-0 Aluminum Alloy (6,7).

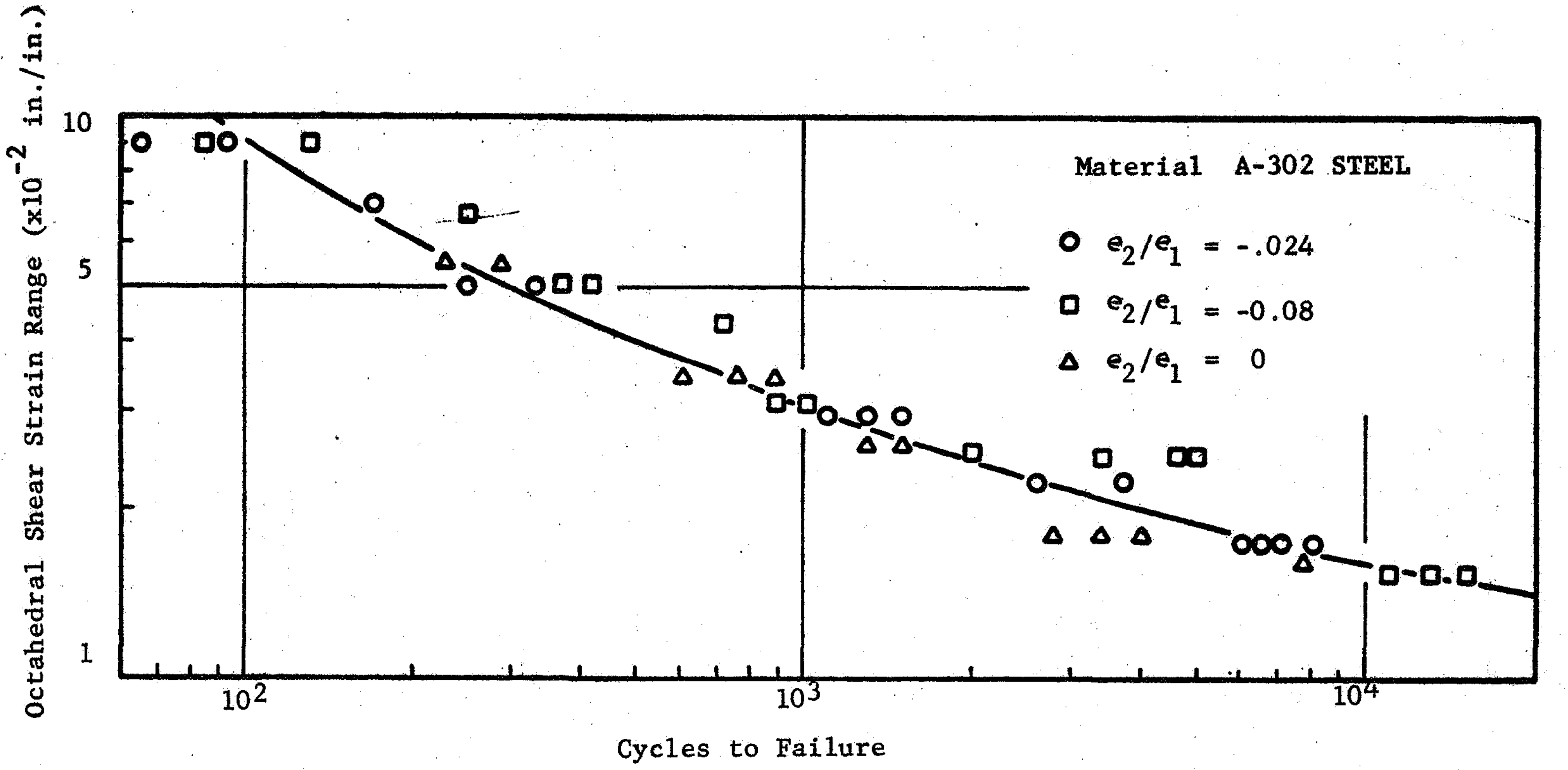

Figure 14. Comparison of Low-Cycle Fatigue Data Obtained Under Different Strain Multiaxialities Based on Octahedral Shear Strain for A-302 Steel (6,7).

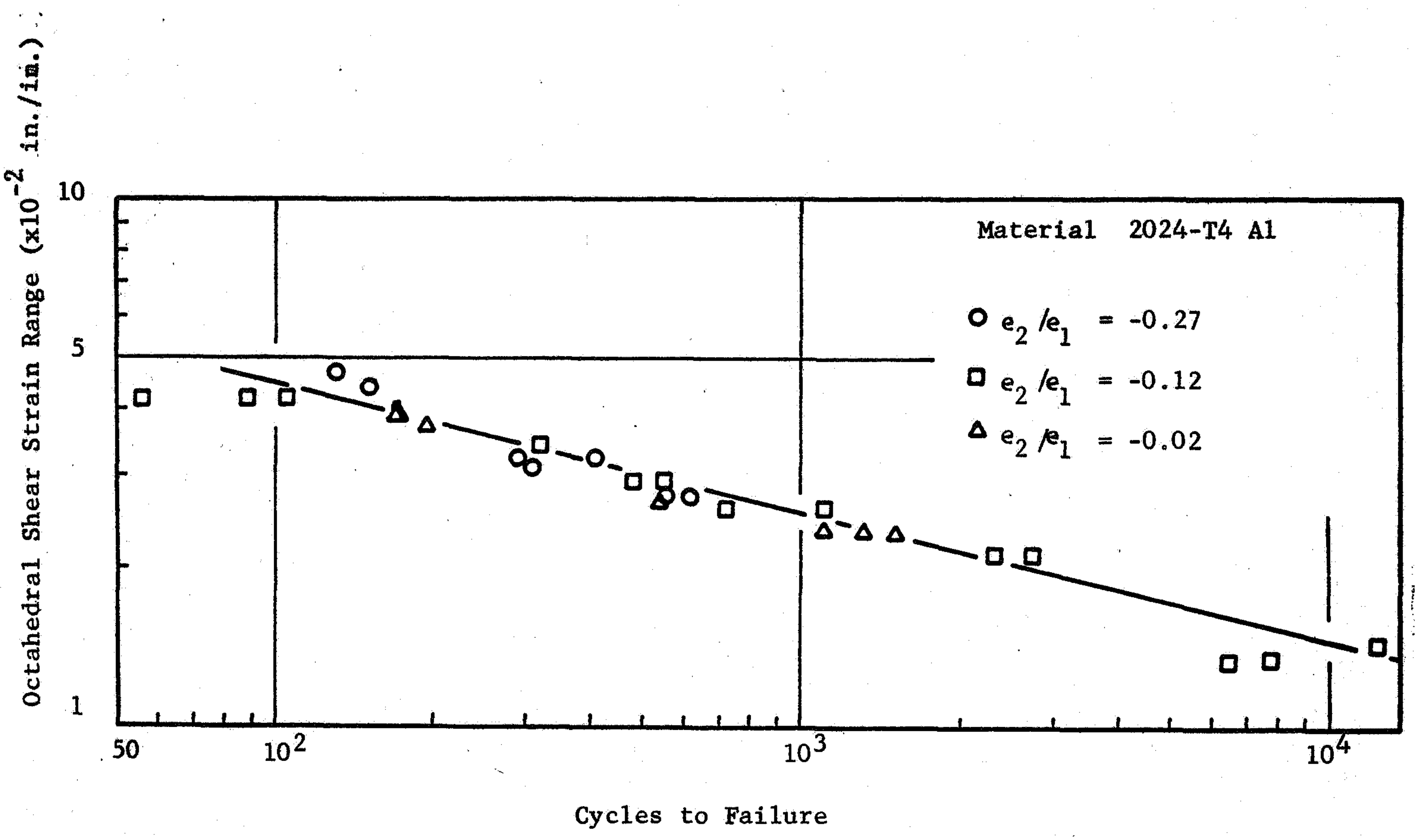

Figure 15. Comparison of Low-Cycle Fatigue Data Obtained Under Different Strain Multiaxialities Based on Octahedral Shear Strain for 2024-T4 Aluminum Alloy (6,7).

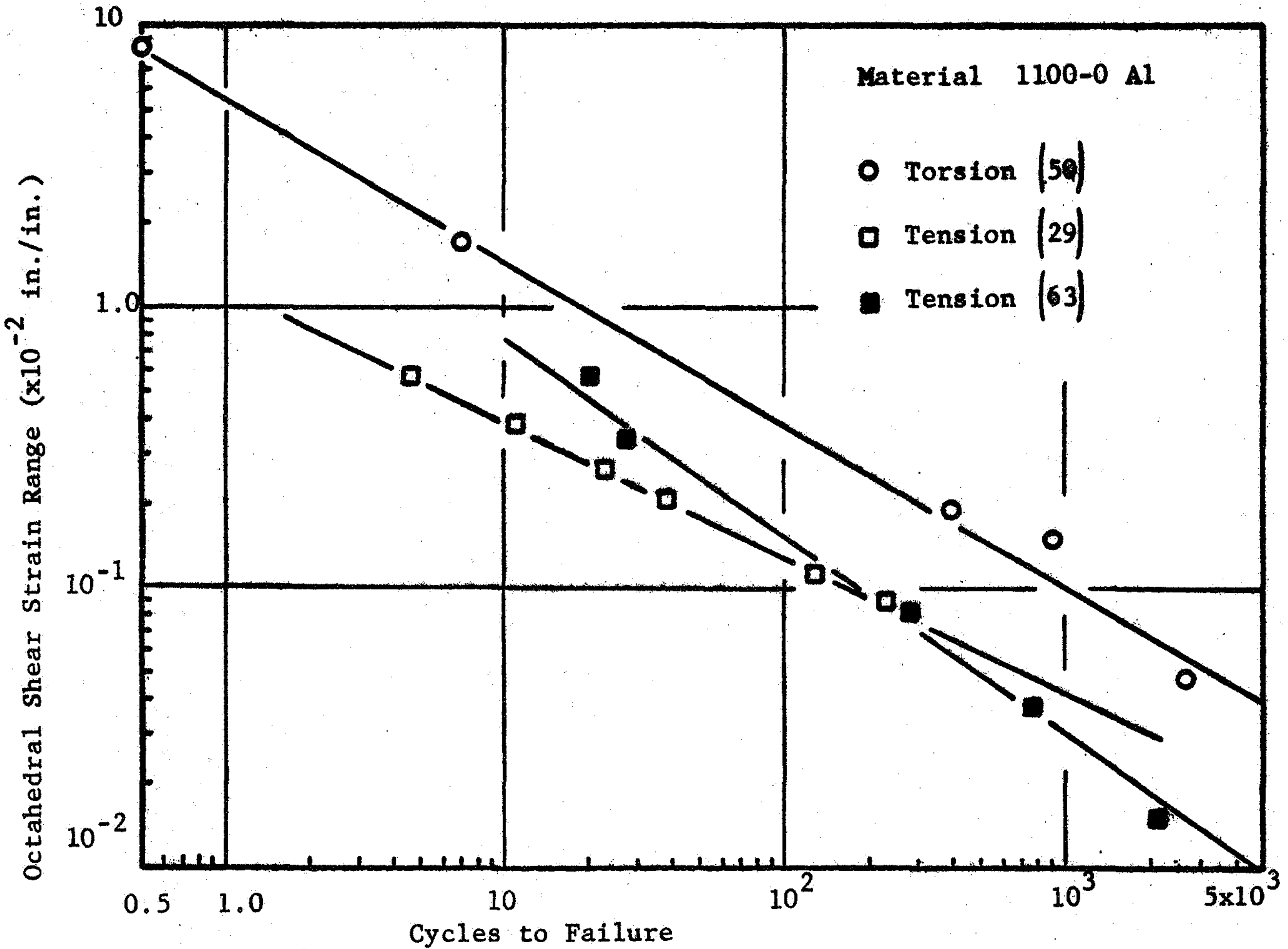

Figure 16. Comparison of Torsional and Axial Strain-Cycling Data Based on Octahedral Shear Strain for 1100-0 Aluminum Alloy

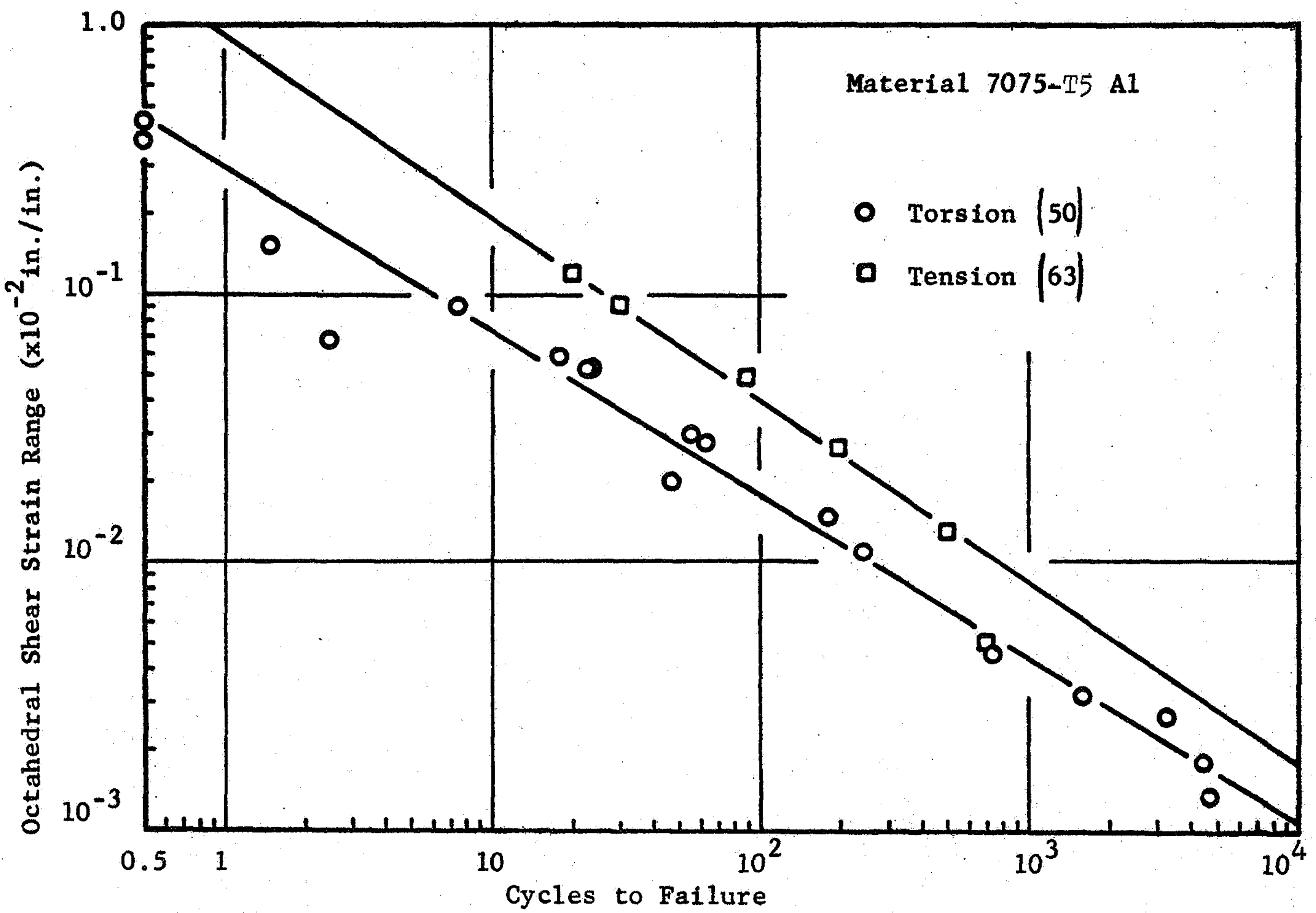

Figure 17. Comparison of Torsional and Axial Strain-Cycling Data Based on Octahedral Shear Strain for 7075-T5 Aluminum Alloy

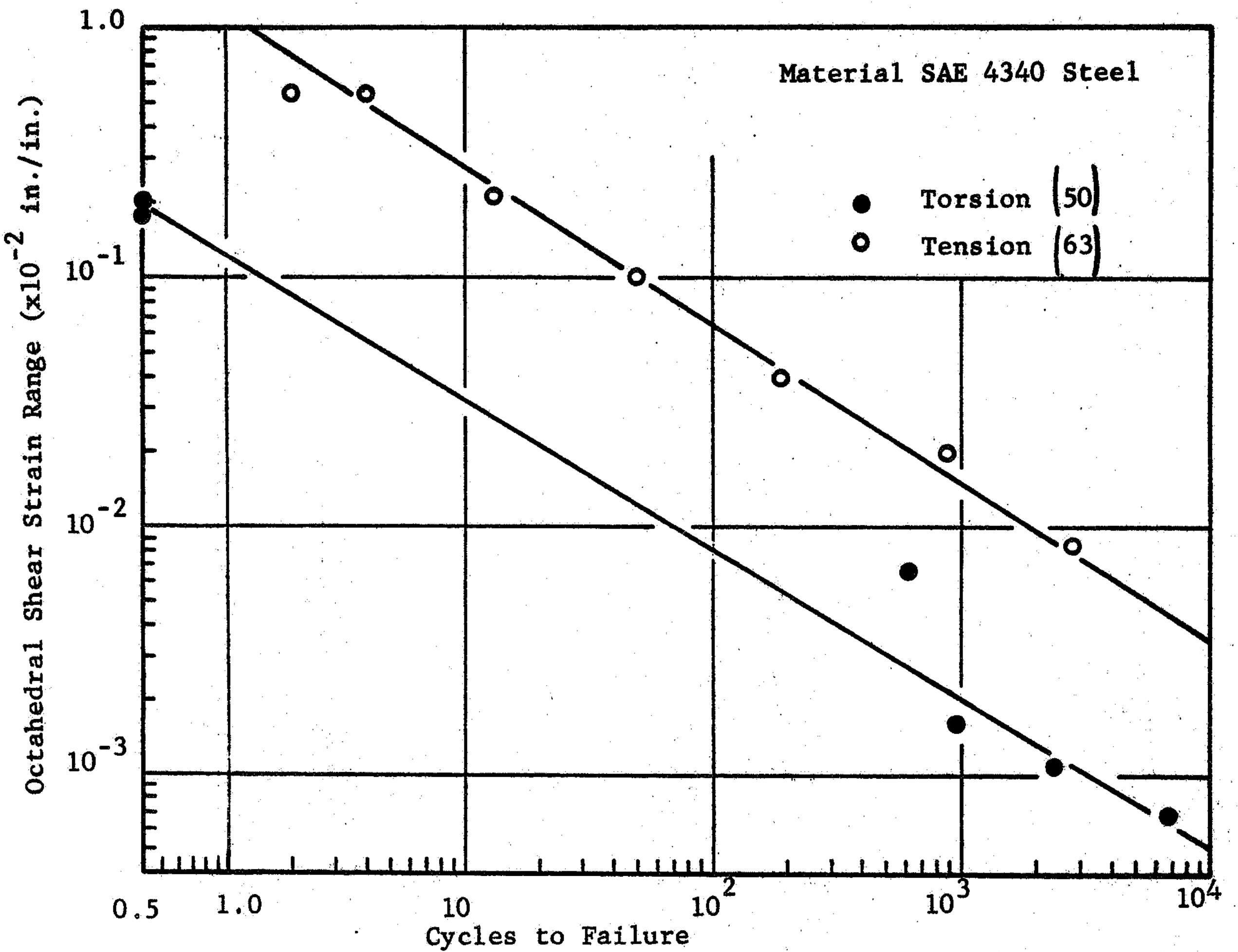

Figure 18. Comparison of Torsional and Axial Data Based on Octahedral Shear Strain for SAE 4340 Steel

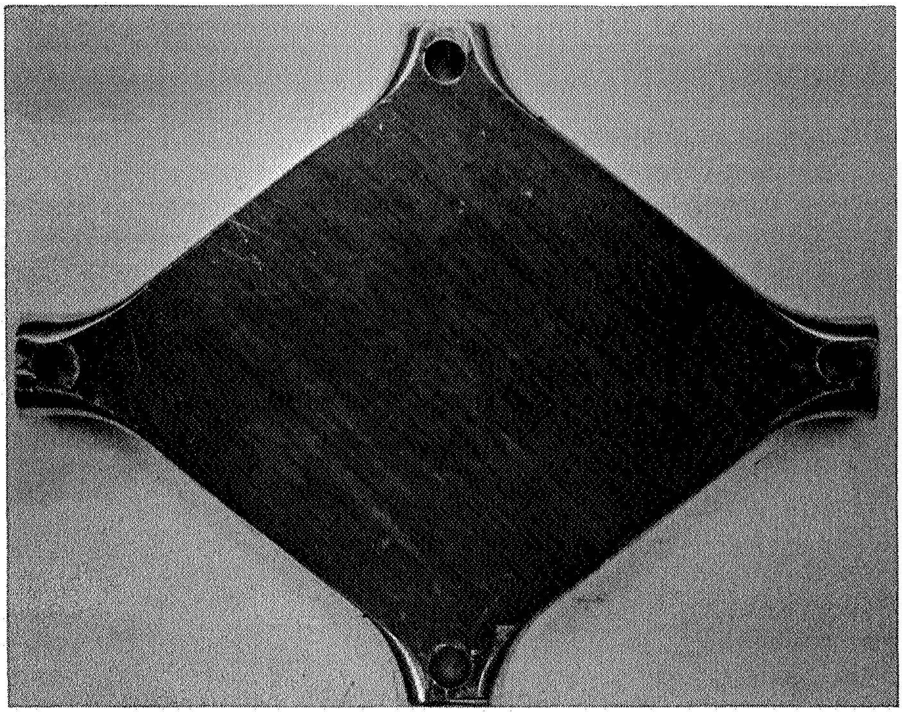

Figure 19. Failed Surface of 2x2.5 Specimen under 1.99 Percent Maximum Strain Range at 450 Cycles

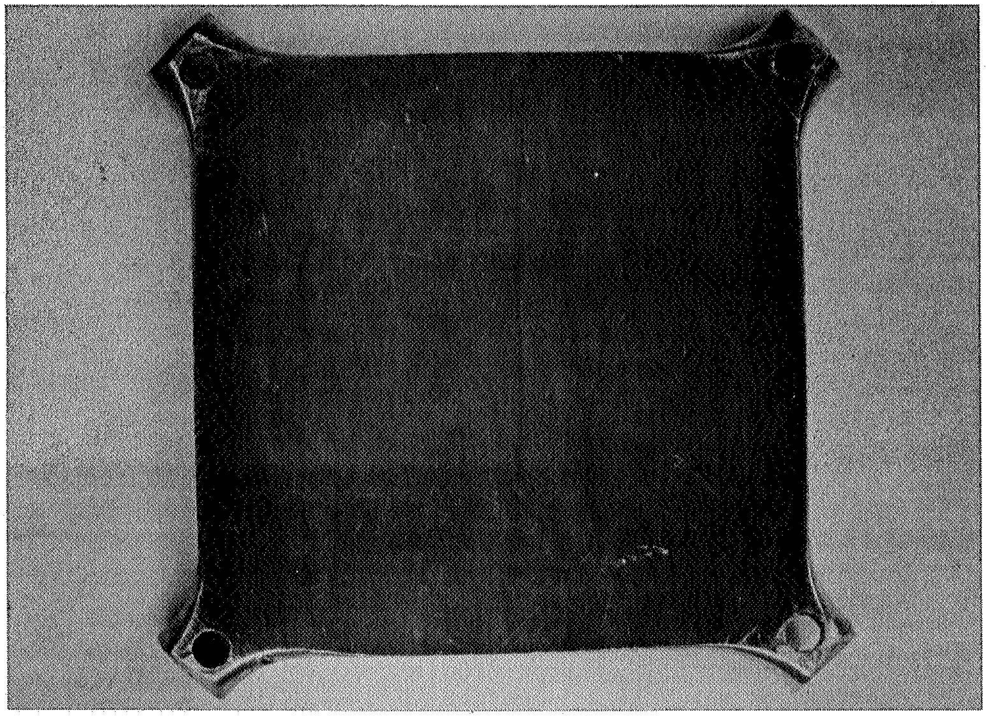

Figure 20. Failed Surface of 3x3 Specimen under 3.50 Percent Maximum Strain Range at 82 Cycles

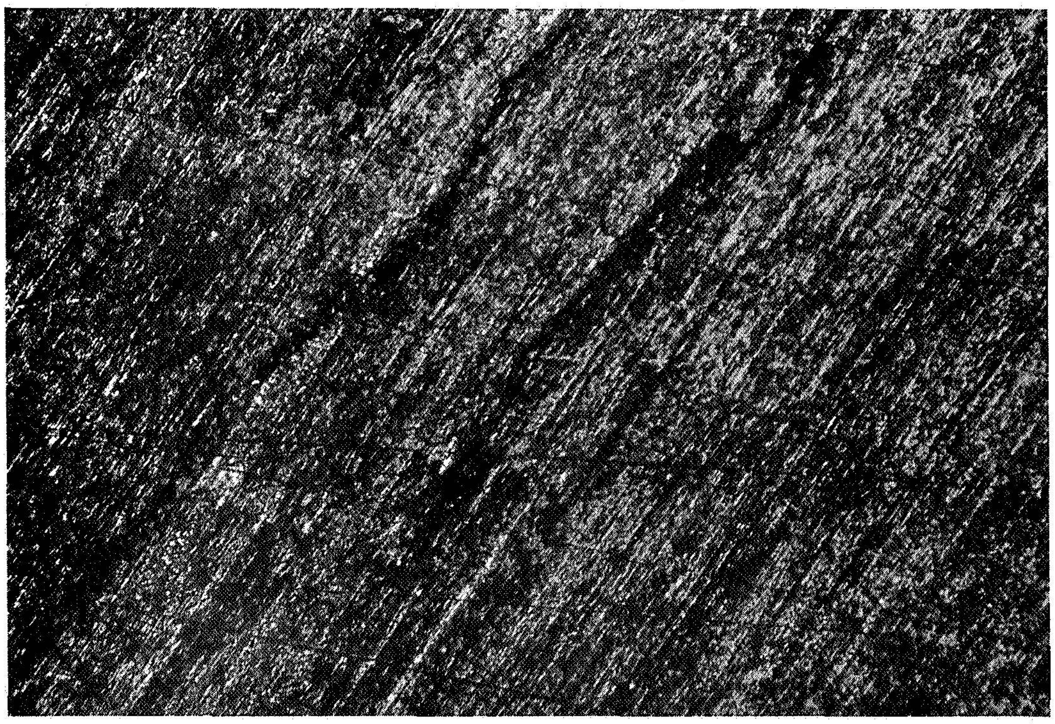

Figure 21. Cracks of 2x2.5 Specimen under 1.99 Percent Maximum Strain Range at 450 Cycles

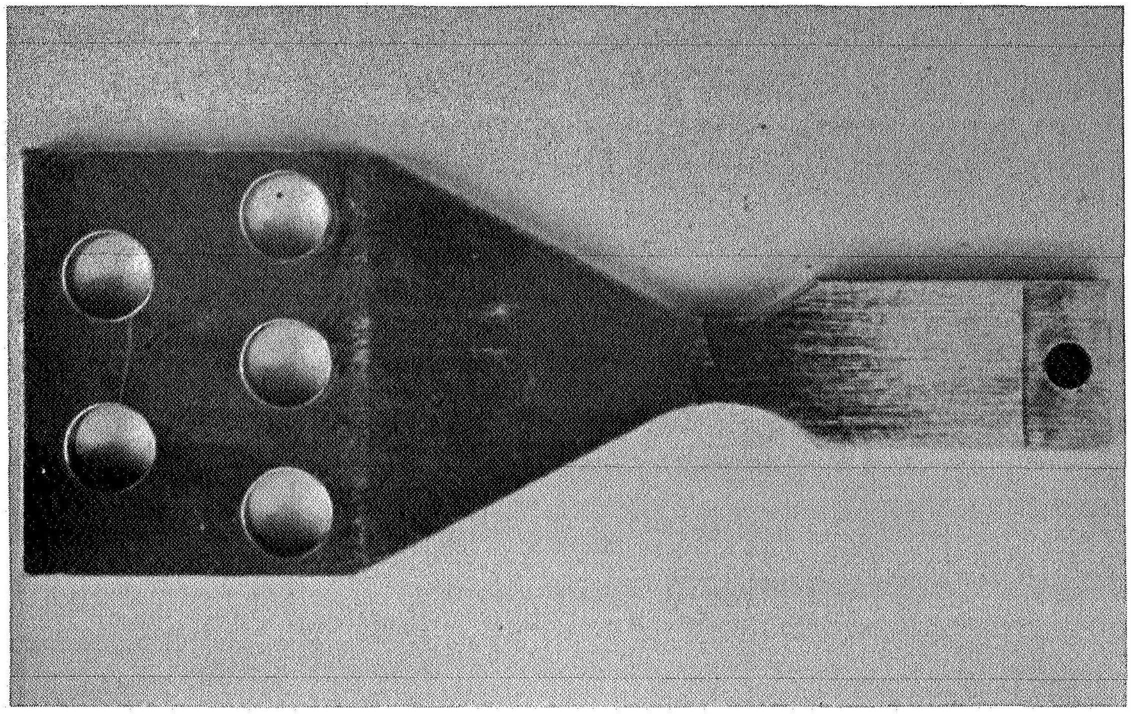

Figure 22. Failed Surface of Cantilever Specimen under 3.50 Percent Maximum Strain Range at 113 Cycles

14. References

1. Gross, J. H., D. E. Gucer and R. D. Stout. "The Plastic Fatigue Strength of Pressure Vessel Steels," The Welding Journal, Vol. 33, No. 1, Research Suppl., 1954, pp. 31-S to 39-S.

2. Gross, J. H., S. Tsang and R. D. Stout. "Factors Affecting Resistance of Pressure Vessel Steels to Repeated Overloading," The Welding Journal, Vol. 32, Research Suppl., 1953, pp. 23-S to 30-S.

3. Gross, J. H. and R. D. Stout. "Plastic Fatigue Properties of High Strength Pressure-Vessel Steels," The Welding Journal, Vol. 34, Research Suppl., 1955, pp. 161-S to 166-S.

4. Tör, S. S., J. M. Ruzek and R. D. Stout. "Repeated Load Tests on Welded and Prestrained Steels," The Welding Journal, Vol. 31, No. 5, Research Suppl., 1952, pp. 238-S to 246-S.

5. Sachs, G. and V. Weiss. "Beitrage zur Kurzzeitermudung," Zeitschrift für Metallkunde, Fol. 53, 1962, pp. 37-47.

6. Sachs, G., W. W. Gerberich, V. Weiss and J. V. Latorre. "Low-Cycle Fatigue of Pressure-Vessel Materials," ASME Proc., Vol. 60, 1961, pp. 512-529.

7. Weiss, V., J. Sessler and P. Packman. "Effect of Several Parameters on Low-Cycle Fatigue Behavior," Acta Metallurgica, Vol. 11, No. 7, 1963, pp. 809-816.

8. Blaser, R. U., J. T. Tucker, Jr. and L. F. Kooistra. "Biaxial Fatigue Tests on Flat-Plate Specimens," The Welding Journal, Vol. 31, No. 3, Research Suppl., 1952, pp. 161-S to 168-S.

9. Bowman, C. E. and T. J. Dolan. "Resistance to Low-Alloy Steel Plates to Biaxial Fatigue,: The Welding Journal, Vol. 35, No. 2, Research Suppl., 1956, pp. 102-S to 109-S.

10. Ives, K. D. "Equibiaxial Low-Cycle Fatigue Properties of Typical Pressure-Vessel Steels," Report No. 7548, The Babcock and Wilcox Company Research Center, April, 1964.

11. Shewchuk, J. "Studies in Multiaxial Low Cycle Fatigue and Dynamic Creep," Ph.D. Thesis, Eng.Mechs.Dept.,Pennsylvania State Univ.

12. Timoshenko, S. "Strength of Materials," Part 1, D. Van Nostrand Co., Inc., New York, 1956.

13. Manson, S. S. "Behavior of Materials Under Conditions of Thermal Stress," NACA TN 2933, July, 1953.

14. Manson, S. S. and M. H. Hirschberg. "Fatigue Behavior in Strain Cycling in the Low and Intermediate Cycle Range," the 10th Sagamore Army Materials Research Conference, Sagamore, N.Y., August, 1963.

15. Halford, G. R. and J. D. Morrow. "Low-Cycle Fatigue in Torsion," ASTM Proc. Vol. 62, 1963, pp. 695-707.

16. Tavernelli, J. F. and L. F. Coffin, Jr., "A Compilation and Interpretation of Cyclic Strain Fatigue Tests on Metals," ASM Trans., Vol. 51, 1959, pp. 438-453.

17. Benahm, P. P. "Torsional-Strain-Cycling Fatigue of Copper at Low Endurance," Journal of Institute of Metals, Vol. 91, 1962-1963, pp. 404-407.

APPENDIX A

Specimens and Test Results

Table 2. Results of Biaxial Strain-Cycling for 3x3 Specimens

No.	Deflection Amplitude, W (inch)	Maximum Strain Range, Δe_1 (in/in)	Strain Ratio ϕ	Maximum Shear Strain Range, $\Delta\gamma_{max}$ (in/in)	Octahedral Shear Strain Range, $\Delta\gamma_{oct}$ (in/in)	Number of Cycles to Failure, N
		$\times 10^{-2}$		$\times 10^{-2}$	$\times 10^{-2}$	
1	0.124	1.12	-1.0	1.12	1.83	1700
2	0.125	1.13	-1.0	1.13	1.84	1490
3	0.125	1.13	-1.0	1.13	1.84	1850
4	0.170	1.60	-1.0	1.60	2.61	495
5	0.175	1.65	-1.0	1.65	2.69	450
6	0.175	1.65	-1.0	1.65	2.69	500
7	0.250	2.50	-1.0	2.50	4.08	170
8	0.252	2.52	-1.0	2.52	4.11	162
9	0.252	2.52	-1.0	2.52	4.11	180
10	0.345	3.45	-1.0	3.45	5.62	78
11	0.345	3.45	-1.0	3.45	5.62	80
12	0.350	3.50	-1.0	3.50	5.71	80
13	0.395	3.95	-1.0	3.95	6.44	58
14	0.400	4.00	-1.0	4.00	6.52	62
15	-	-	-	-	-	-

Table 3. Results of Biaxial Strain-Cycling for 2x2 Specimens

No.	Deflection Amplitude, W inch	Maximum Strain Range, Δe_1 (in/in)	Strain Ratio ϕ	Maximum Shear Strain Range, $\Delta\gamma_{max}$ (in/in)	Octahedral Shear Strain Range, $\Delta\gamma_{oct}$ (in/in)	Number of Cycles to Failure N
		$\times 10^{-2}$		$\times 10^{-2}$	$\times 10^{-2}$	
1	0.07	1.64	-1	1.64	2.68	1160
2	0.07	1.64	-1	1.64	2.68	1100
3	0.071	1.65	-1	1.65	2.70	1090
4	0.103	2.46	-1	2.46	4.01	352
5	0.105	2.48	-1	2.48	4.05	312
6	0.105	2.48	-1	2.48	4.05	295
7	0.150	3.60	-1	3.60	5.87	112
8	0.153	3.64	-1	3.64	5.94	108
9	0.155	3.66	-1	3.66	5.98	103
10	0.200	4.80	-1	4.80	7.83	64
11	0.203	4.86	-1	4.86	7.93	64
12	0.204	4.88	-1	4.88	7.96	60

Table 4. Results of Biaxial Strain-Cycling for 2x2.5 Specimens

No.	Deflection Amplitude, W (inch)	Maximum Strain Range, Δe_1 (in/in)	Strain Ratio ϕ	Maximum Shear Strain Range, $\Delta\gamma_{max}$ (in/in)	Octahedral Shear Strain Range, $\Delta\gamma_{oct}$ (in/in)	Number of Cycles to Failure, N
		$\times 10^{-2}$		$\times 10^{-2}$	$\times 10^{-2}$	
1	0.080	1.45	-0.86	1.35	2.08	1412
2	0.080	1.45	-0.86	1.35	2.08	1060
3	0.105	1.95	-0.89	1.83	2.87	403
4	0.107	1.99	-0.89	1.88	2.93	370
5	0.111	2.05	-0.89	1.90	3.01	351
6	0.149	-	-	-	-	-
7	0.151	2.83	-0.90	2.69	4.20	135
8	0.157	2.96	-0.90	2.81	4.39	159
9	0.200	3.76	-0.91	3.59	5.63	85
10	0.204	3.85	-0.91	3.68	5.76	76
11	0.205	3.86	-0.91	3.69	5.78	72
12	0.300	5.70	-0.92	5.04	8.60	29
13	0.300	5.70	-0.92	5.04	8.60	28
14	0.400	7.65	-0.92	7.35	11.6	16
15	0.400	7.65	-0.92	7.35	11.6	12

Table 5. Results of Biaxial Strain-Cycling for 2x3 Specimens

No.	Deflection Amplitude, W (inch)	Maximum Strain Range, Δe_1 (in/in)	Strain Ratio ϕ	Maximum Shear Strain Range, $\Delta\gamma_{max}$ (in/in)	Octahedral Shear Strain Range, $\Delta\gamma_{oct}$ (in/in)	Number of Cycles to Failure, N
		$\times 10^{-2}$		$\times 10^{-2}$	$\times 10^{-2}$	
1	0.100	1.45	-0.81	1.31	2.00	1100
2	0.102	1.45	-0.81	1.31	2.00	1840
3	0.104	1.45	-0.81	1.31	2.00	1090
4	0.150	2.25	-0.81	2.04	3.10	322
5	0.151	2.25	-0.81	2.04	3.10	292
6	0.155	2.30	-0.81	2.08	3.17	289
7	0.200	3.05	-0.81	2.90	4.21	138
8	0.202	3.06	-0.81	2.91	4.22	143
9	0.203	3.06	-0.81	2.91	4.22	138
10	0.300	4.65	-0.81	4.21	6.41	56
11	0.300	4.65	-0.81	4.21	6.41	51
12	0.300	4.65	-0.81	4.21	6.41	53
13	0.400	6.30	-0.81	5.70	8.69	26
14	0.400	6.30	-0.81	5.70	8.69	30
15	0.400	6.30	-0.81	5.70	8.69	27

Table 6. Results of Uniaxial Strain-Cycling for Cantilever Specimens

No.	Deflection Amplitude, W (inch)	Maximum Strain Range, Δe_1 (in/in)	Strain Ratio ϕ	Maximum Shear Strain Range, $\Delta\gamma_{max}$ (in/in)	Octahedral Shear Strain Range, $\Delta\gamma_{oct}$ (in/in)	Number of Cycles to Failure, N
		$\times 10^{-2}$		$\times 10^{-2}$	$\times 10^{-2}$	
1	0.10	1.40	-0.5	1.05	1.97	1310
2	0.10	1.40	-0.5	1.05	1.97	1440
3	0.10	1.40	-0.5	1.05	1.97	1690
4	0.11	1.60	-0.5	1.20	2.26	813
5	0.12	1.90	-0.5	1.43	2.68	462
6	0.12	1.90	-0.5	1.43	2.68	520
7	0.14	2.55	-0.5	1.91	3.60	233
8	0.14	2.55	-0.5	1.91	3.60	244
9	0.14	2.55	-0.5	1.91	3.60	260
10	0.16	3.50	-0.5	2.63	4.94	104
11	0.16	3.50	-0.5	2.63	4.94	113
12	0.16	3.50	-0.5	2.63	4.94	118
13	0.20	6.00	-0.5	4.50	8.46	27
14	0.20	6.00	-0.5	4.50	8.46	32
15	0.25	-	-	-	-	-

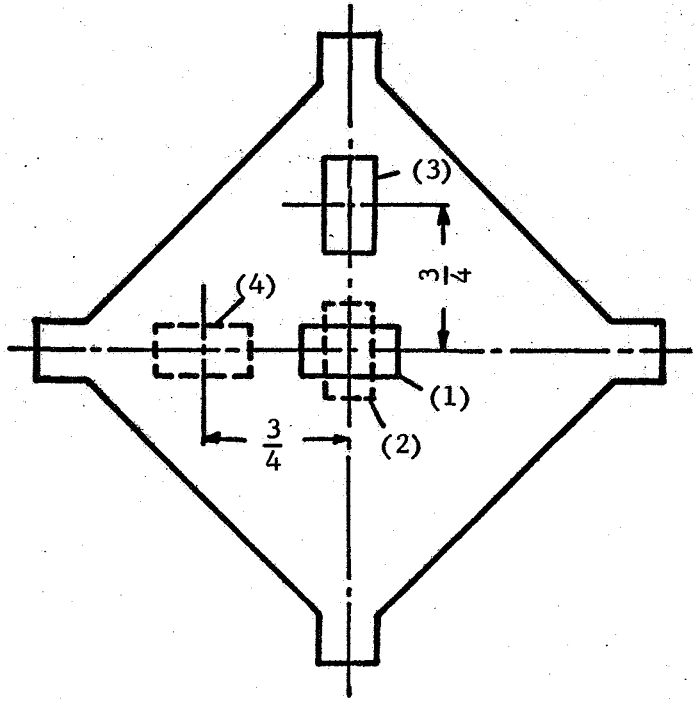

Figure A-1-A. Locations of the Cemented Strain Gages on 3x3 Specimen

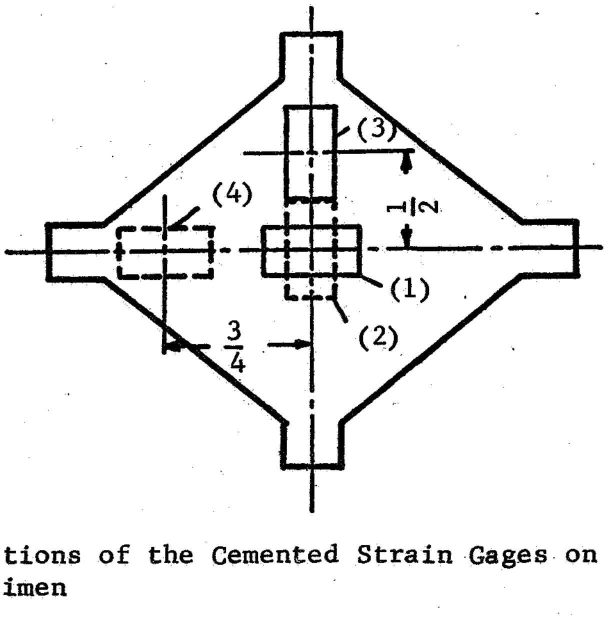

Figure A-1-B. Locations of the Cemented Strain Gages on 2x2.5 Specimen

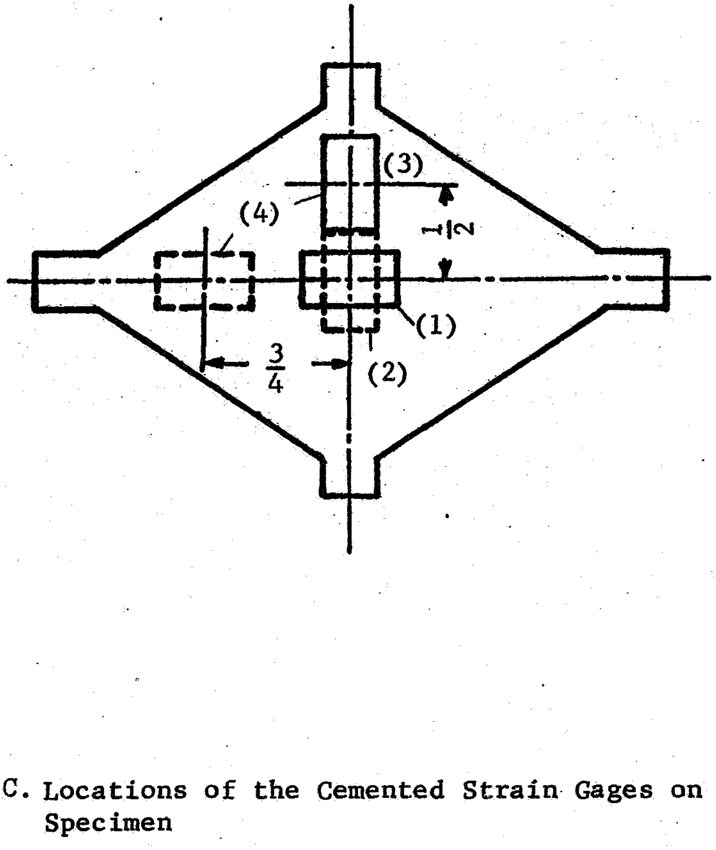

Figure A-1-C. Locations of the Cemented Strain Gages on 2x3 Specimen

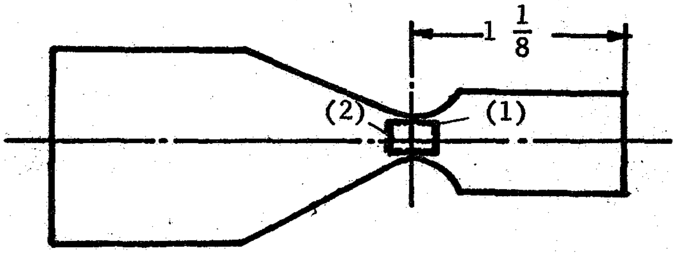

Figure A-1-D. Locations of Cemented Strain Gages on Cantilever Specimens

APPENDIX B

Calibration Tests

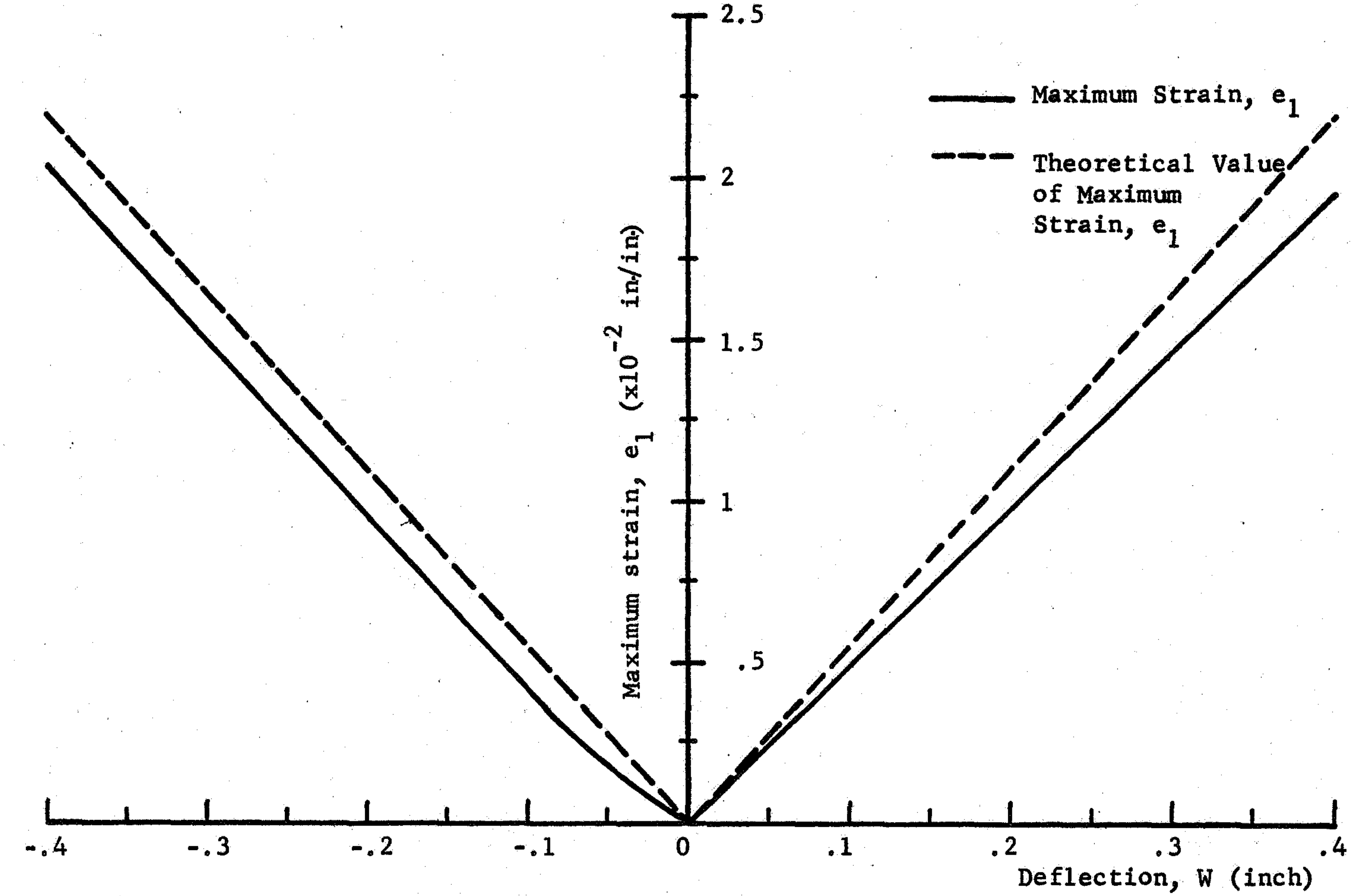

Figure B-1. Maximum Strain vs. Deflection for 3x3 Specimen

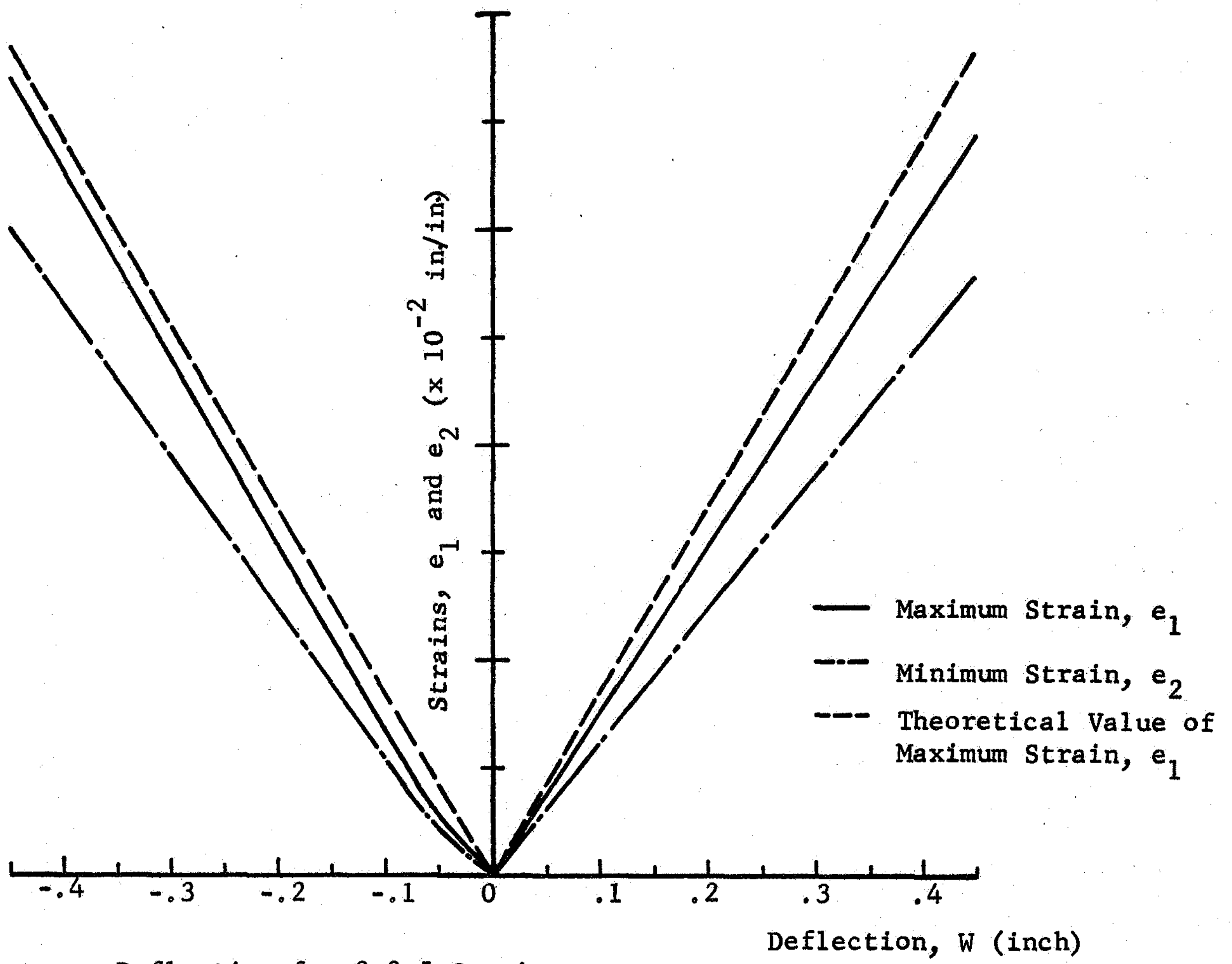

Figure B-2. Strains vs. Deflection for 2x2.5 Specimen

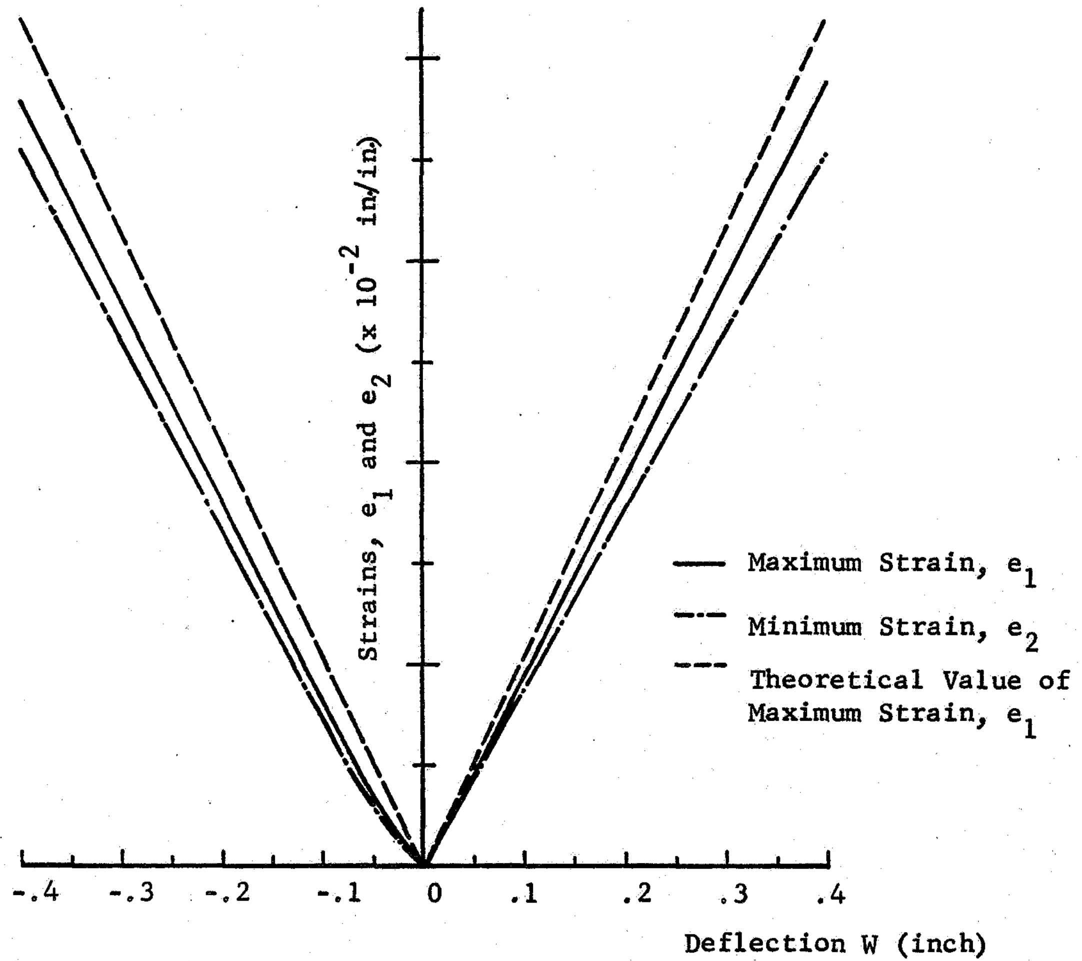

Figure B-3. Strains vs. Deflection for 2x3 Specimen

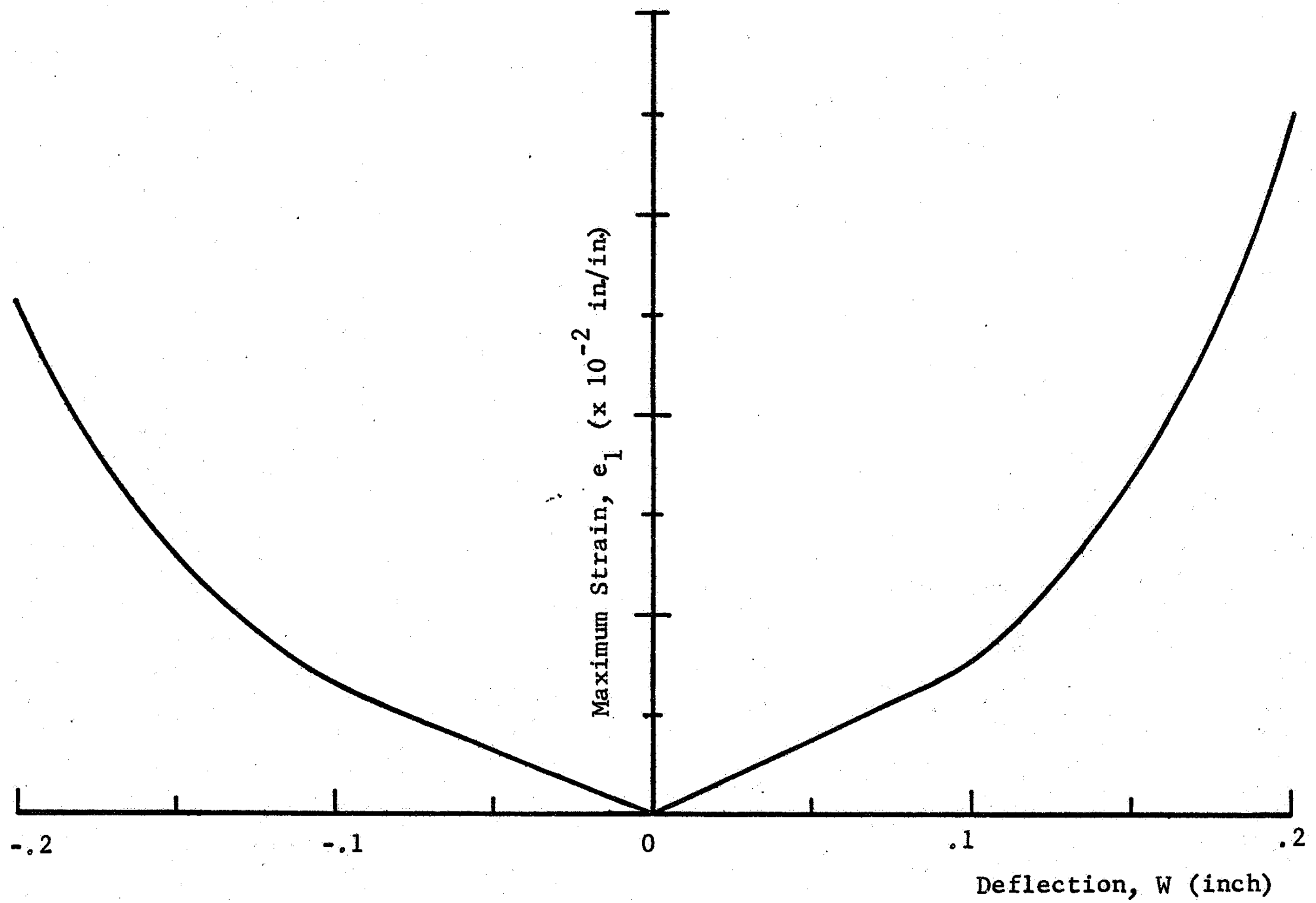

Figure B-4. Maximum Strain vs. Deflection for Cantilever Specimen.

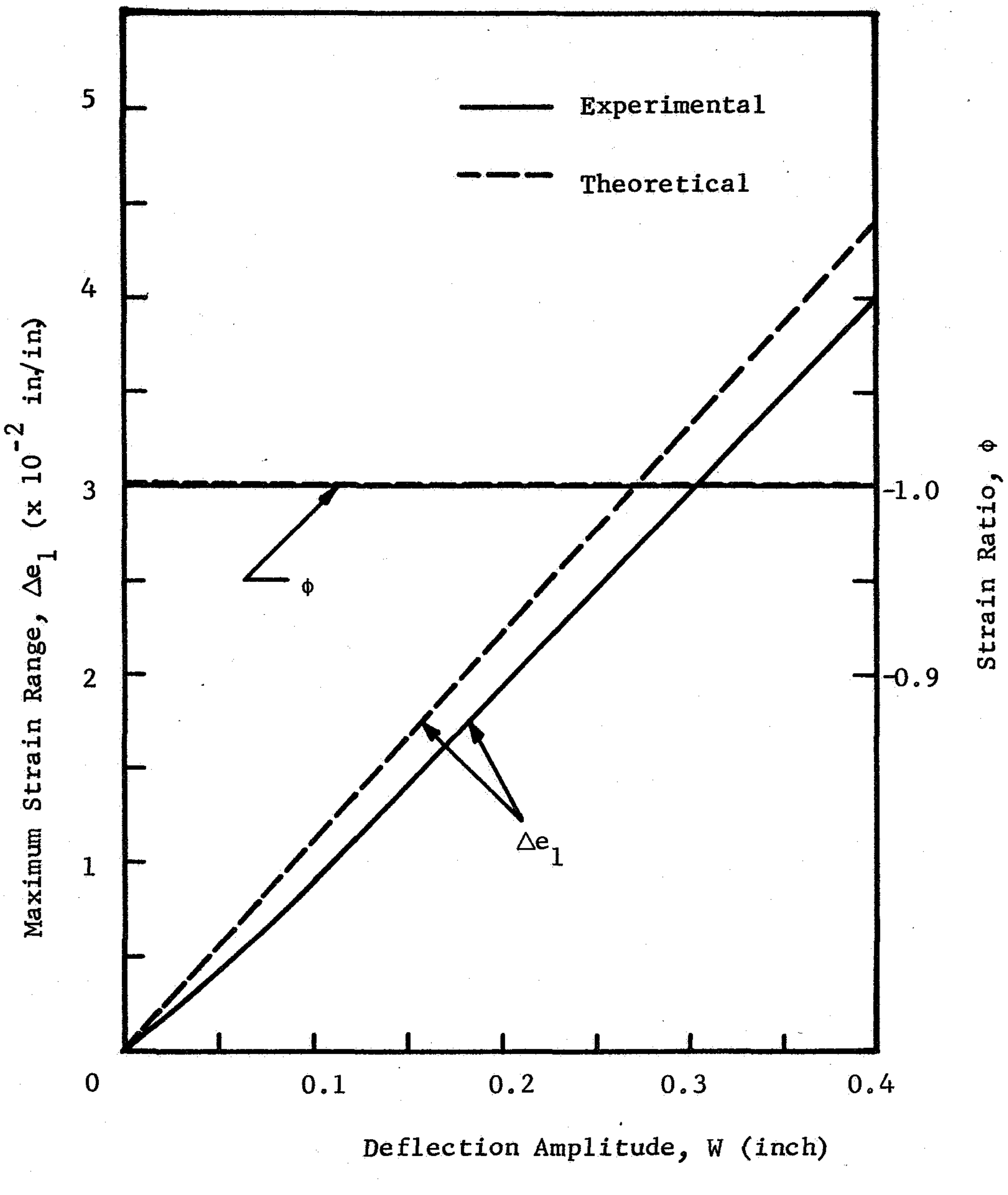

Figure B-5. Maximum Strain Range and Strain Ratio vs. Deflection Amplitude for 3x3 Specimen

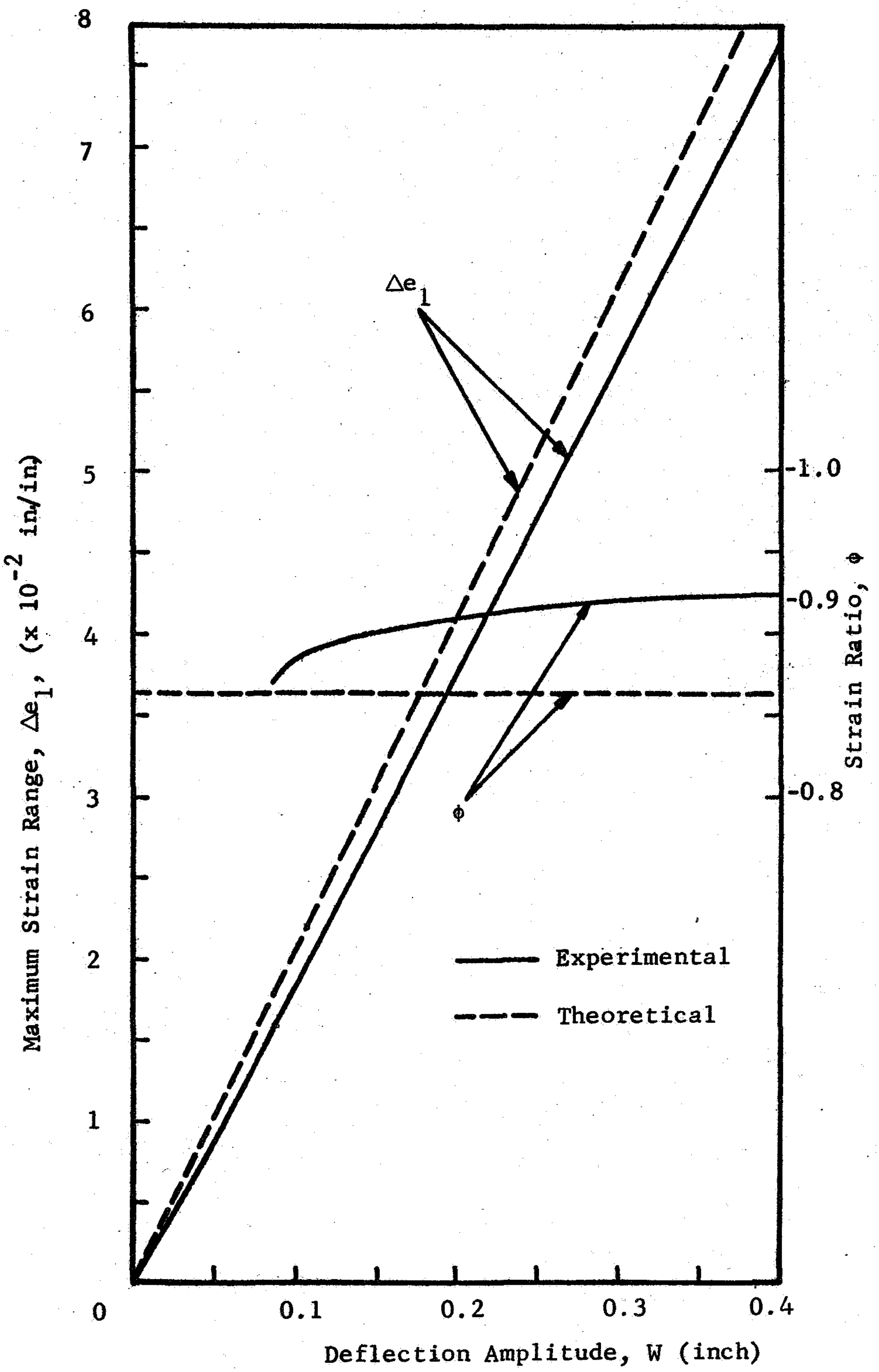

Figure B-6. Maximum Strain Range and Strain Ratio vs. Deflection Amplitude for 2x2.5 Specimen

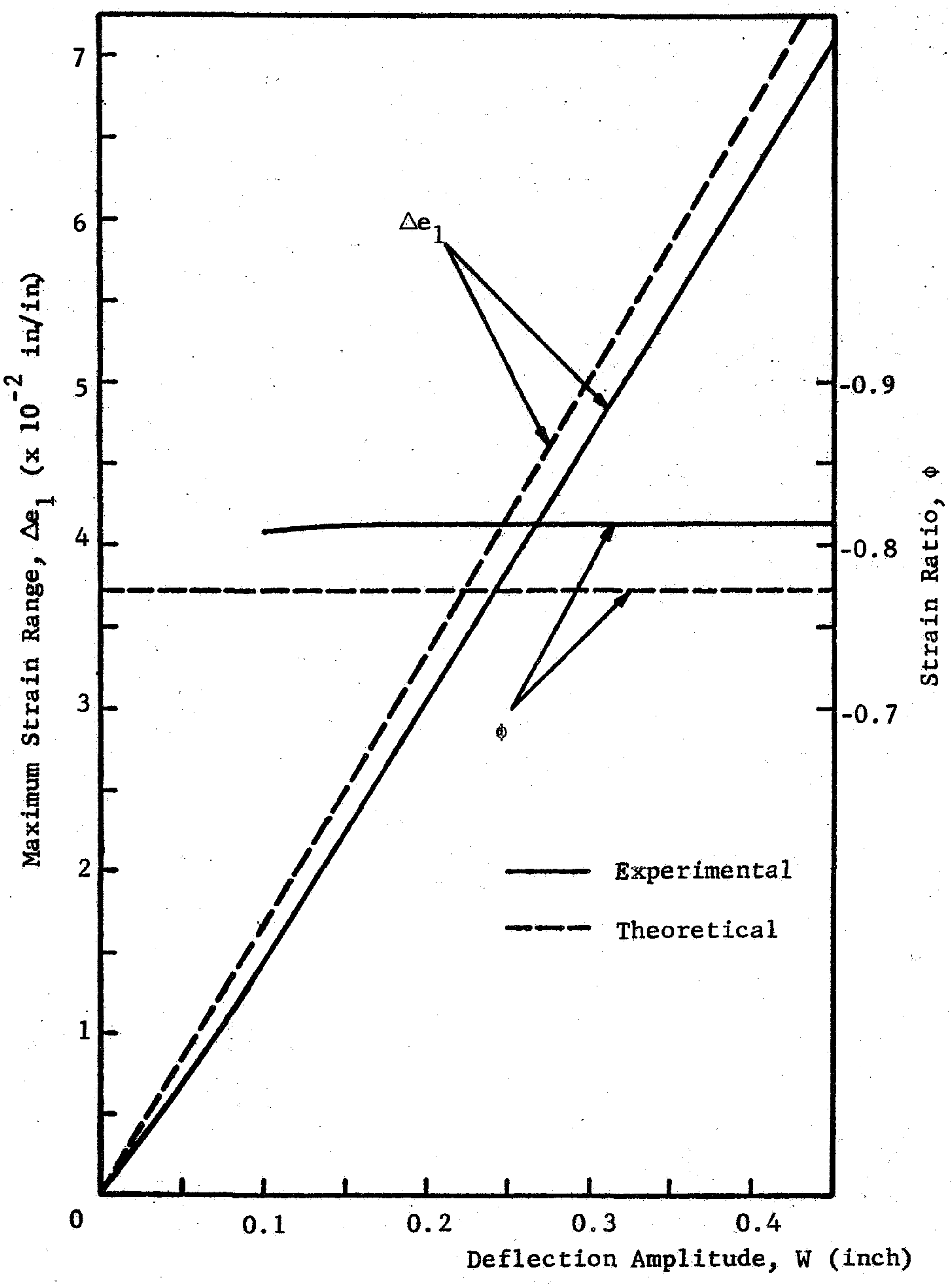

Figure B-7. Maximum Strain Range and Strain Ratio vs. Deflection Amplitude for 2x3 Specimen

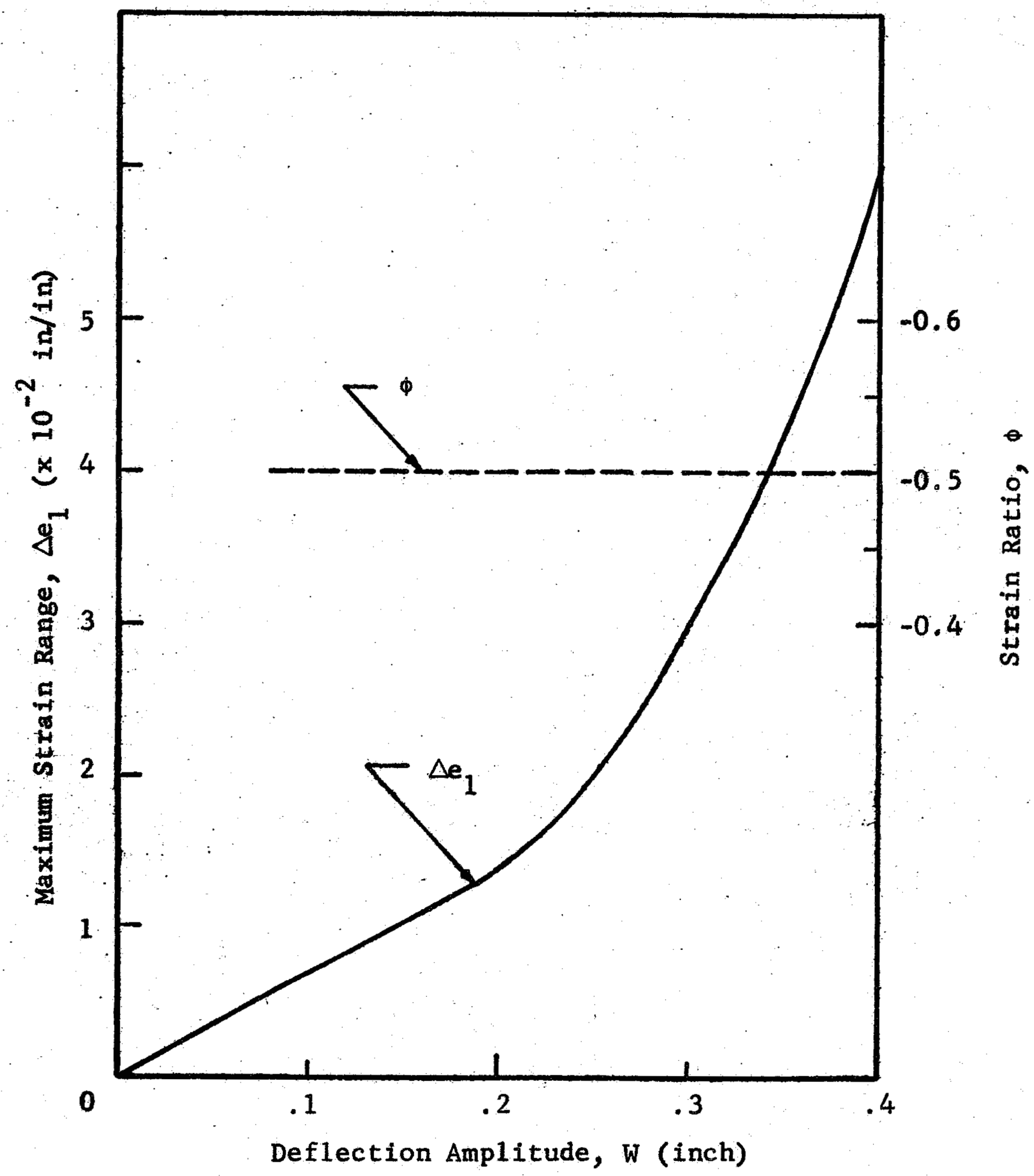

Figure B-8. Maximum Strain Range and Strain Ratio vs. Deflection Amplitude for Cantilever Specimen

APPENDIX C

Testing Equipment

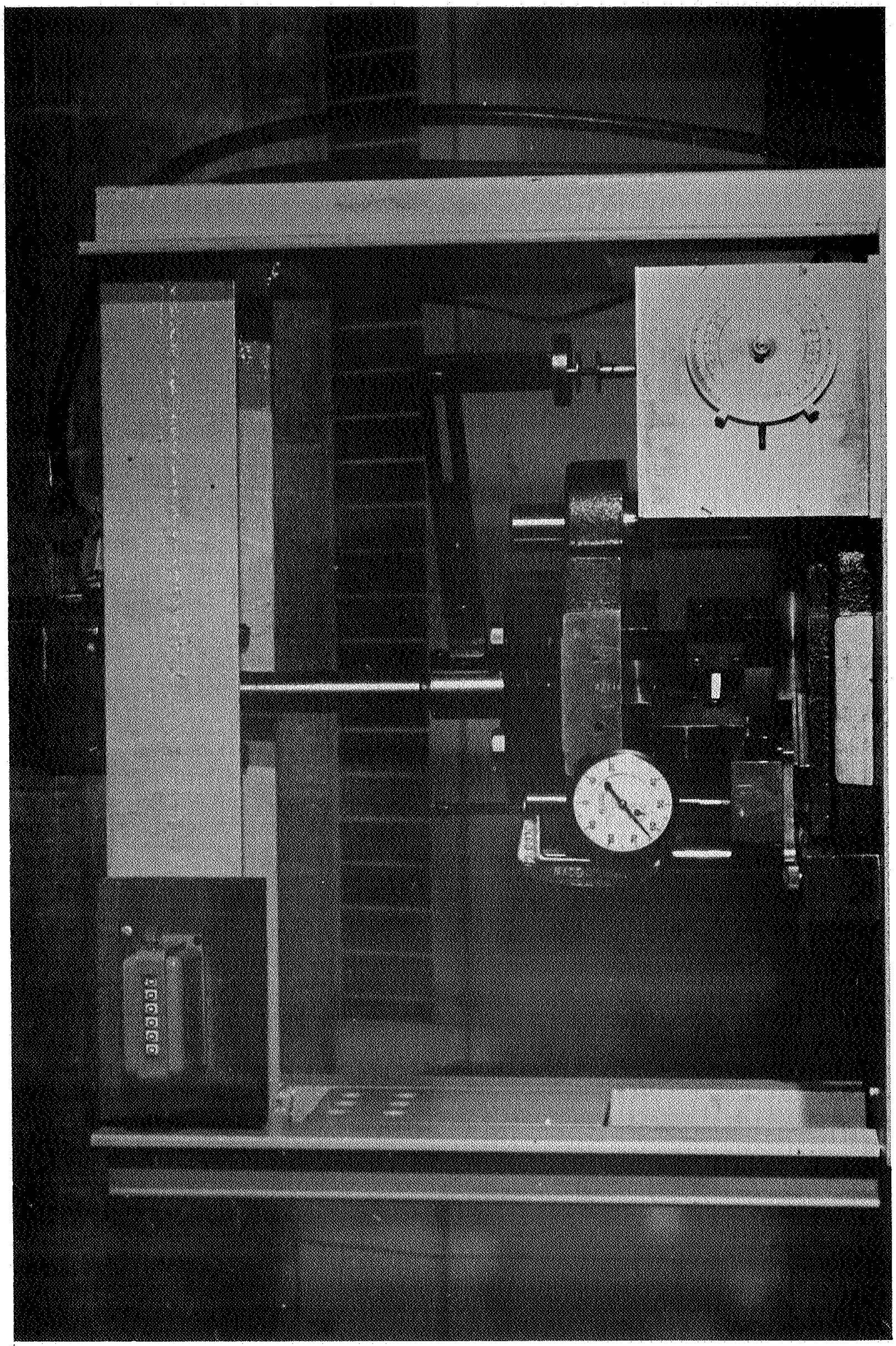

Figure C-1. Testing Machine.

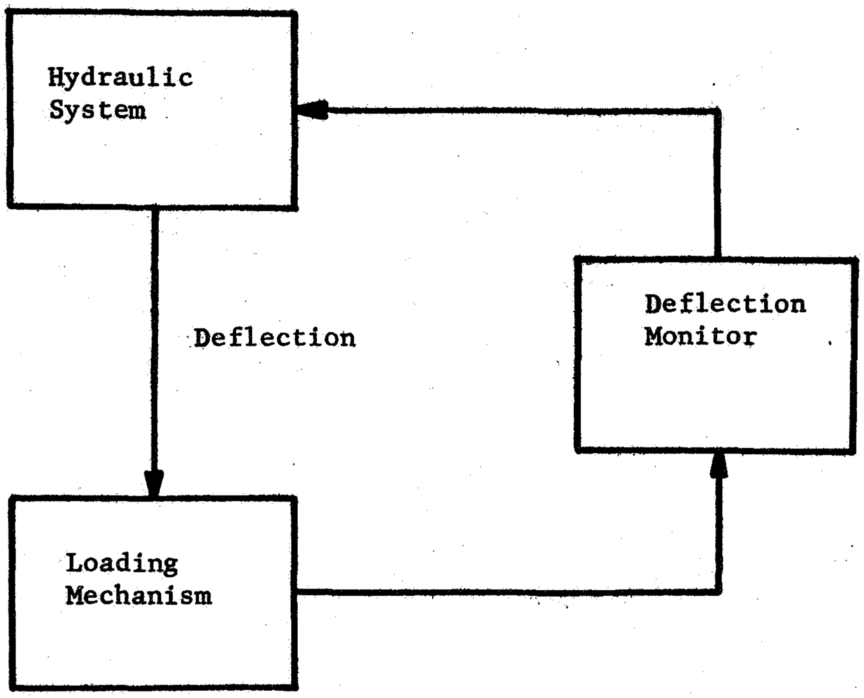

Figure C-2. Schematic Flow Chart of Testing Machine

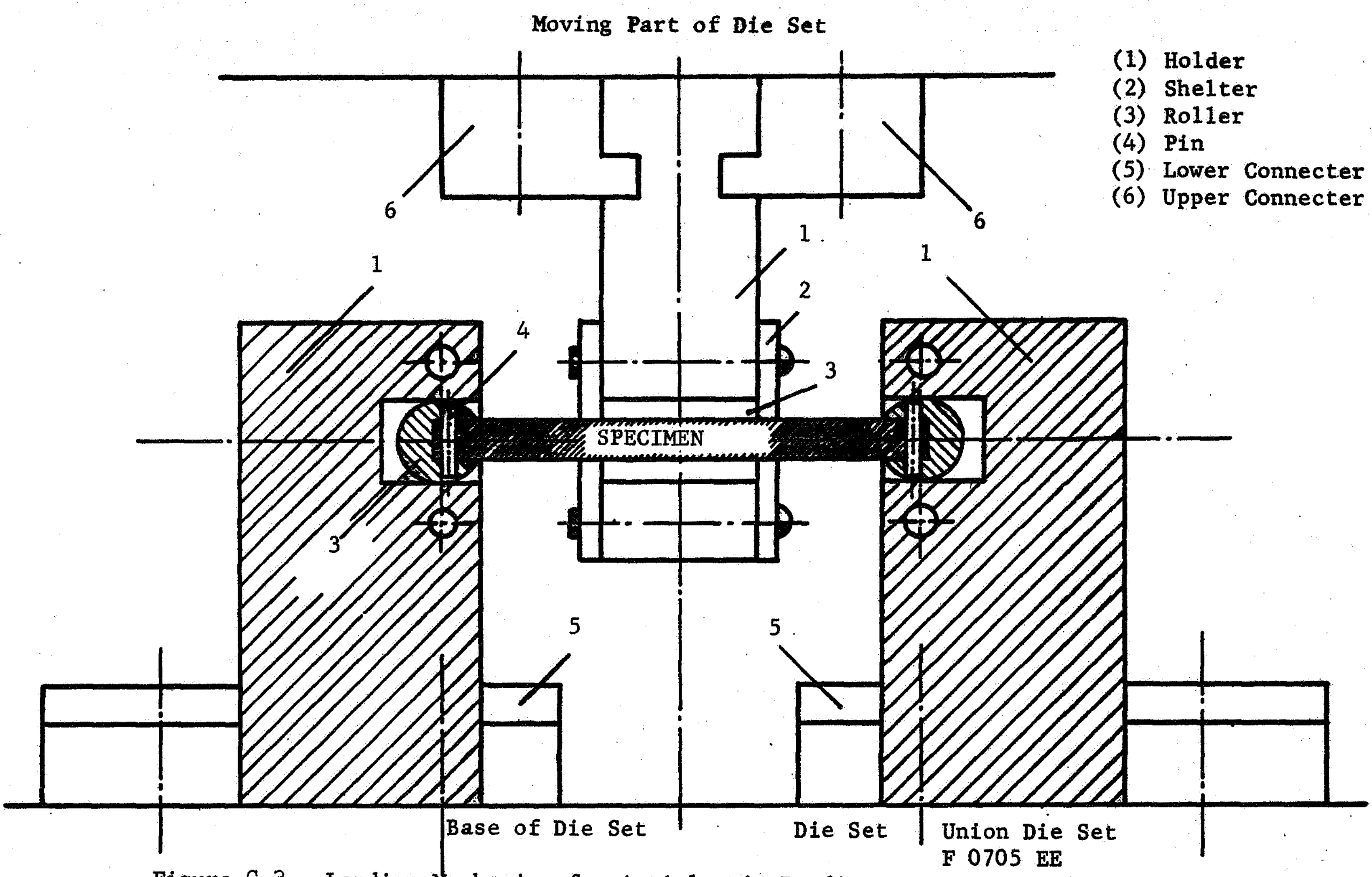

Figure C-3. Loading Mechanism for Anticlastic Bending of Rhombic Specimen

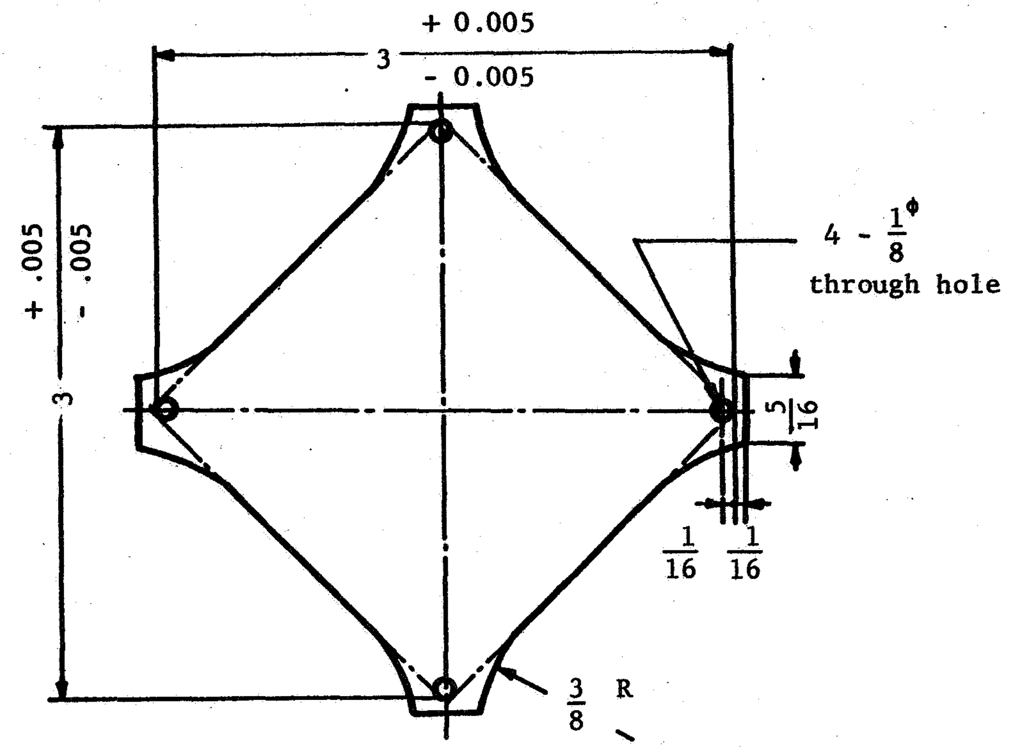

Figure C-4-A. 3 x 3 Rhombic Specimen

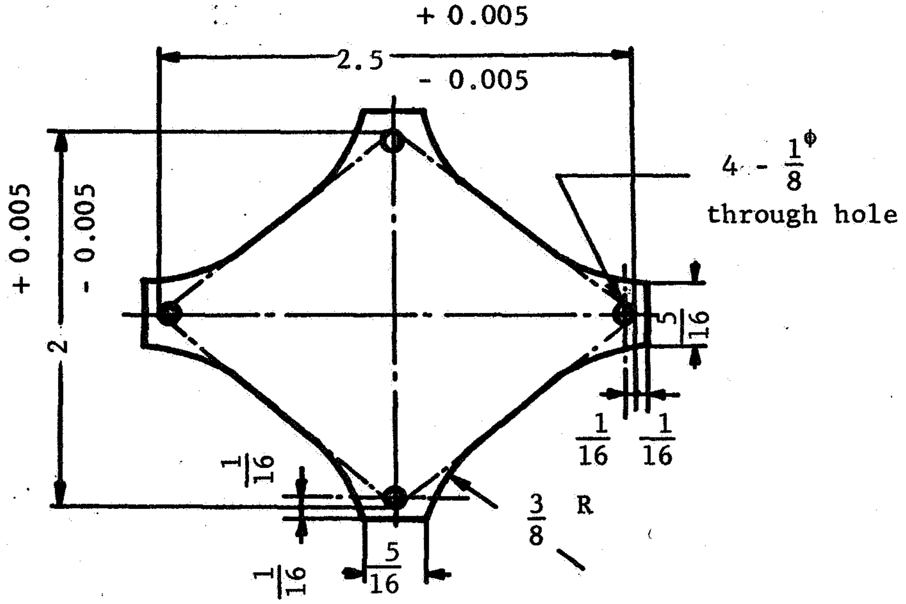

Figure C-4-B. 2x2.5 Rhombic Specimen

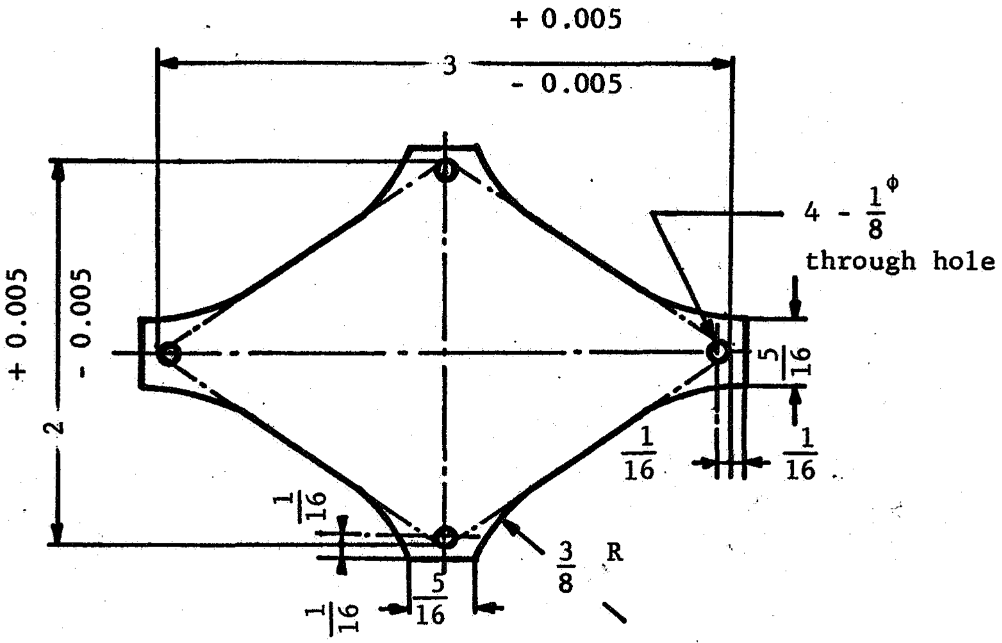

Figure C-4-C. 2 x 3 Rhombic Specimen

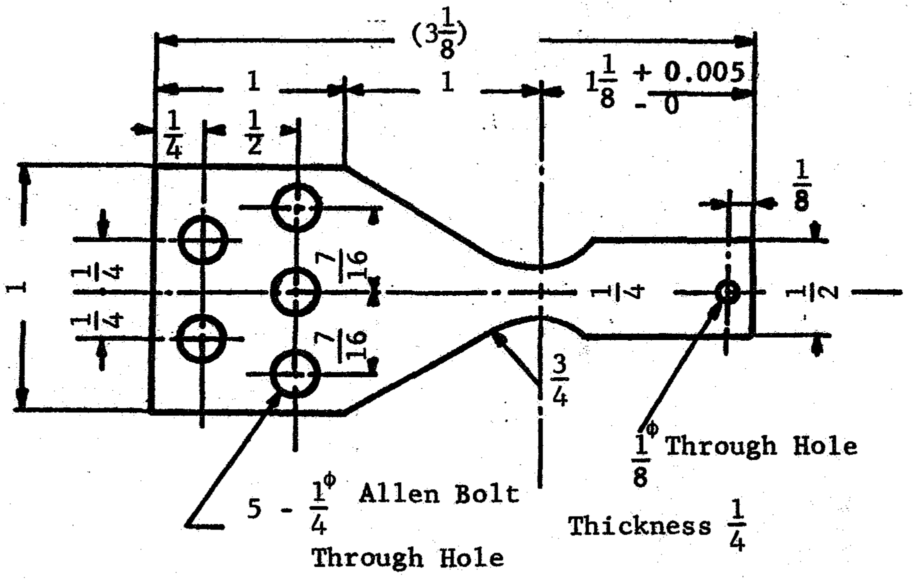

Figure C-5. Cantilever Specimen

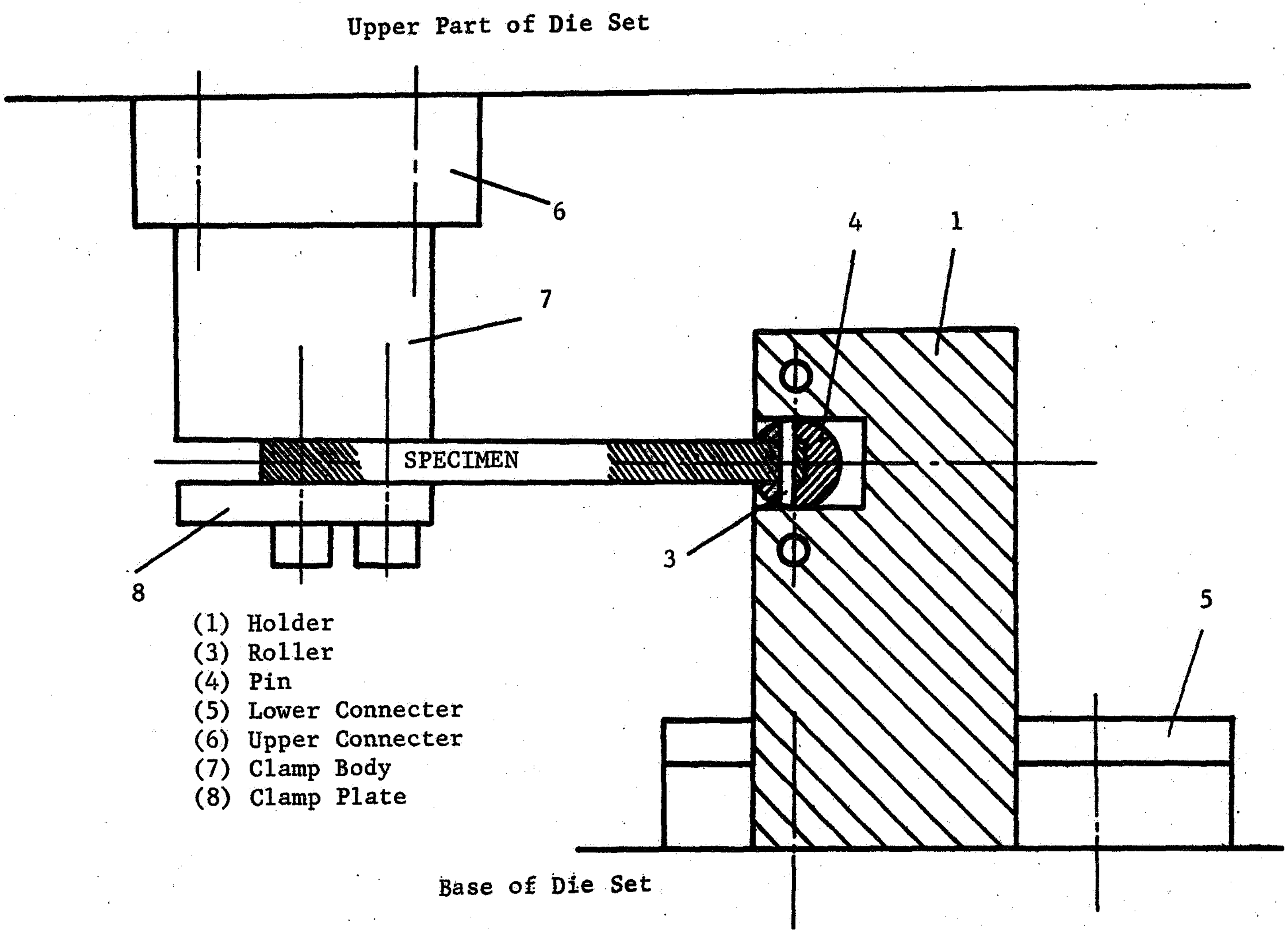

Figure C-6. Loading Mechanism for Cantilever Bending

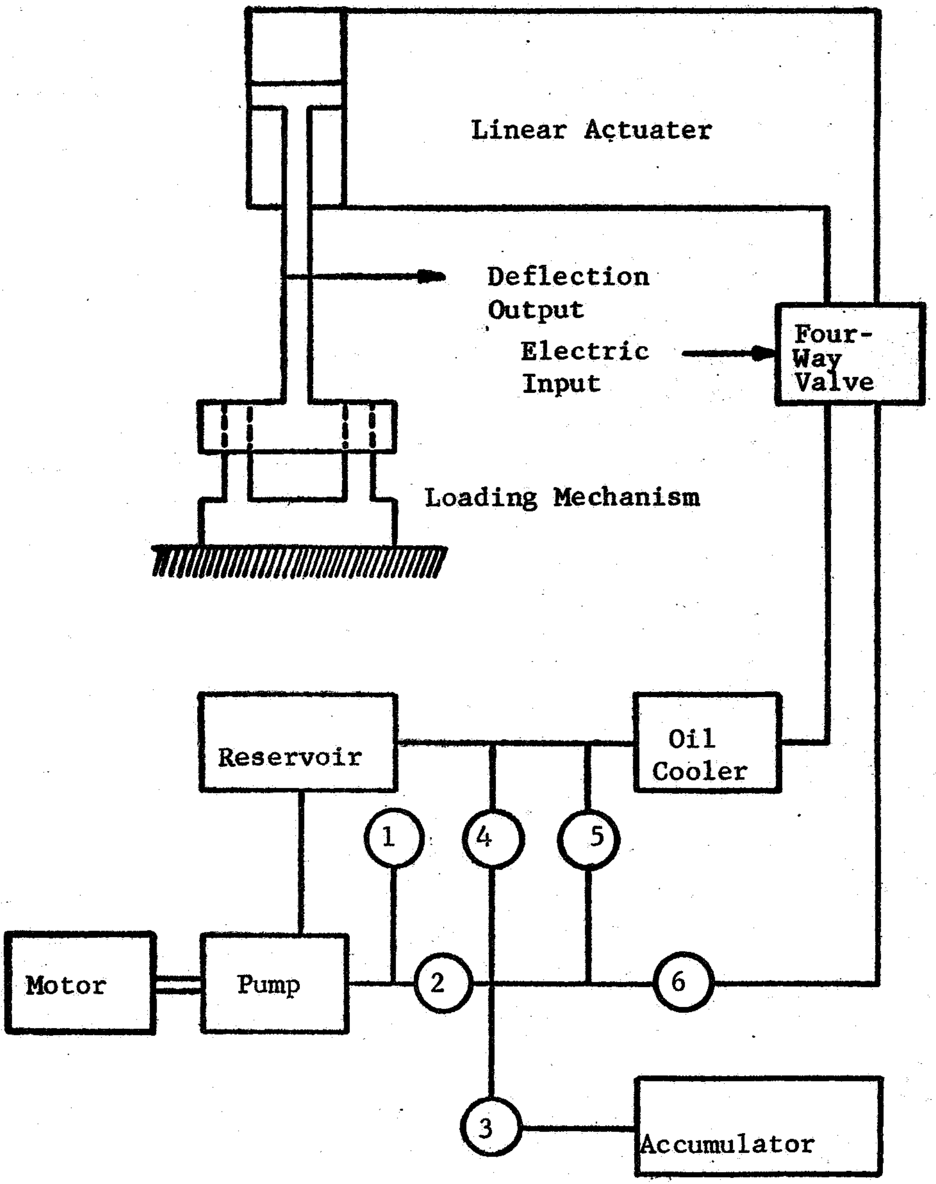

Figure C-7. Schematic Diagram of Hydraulic System

(1) Pressure Gage
(2) Check Valve
(3) Isolation Valve
(4) Relief Valve
(5) Bypass Valve
(6) Throttle Valve

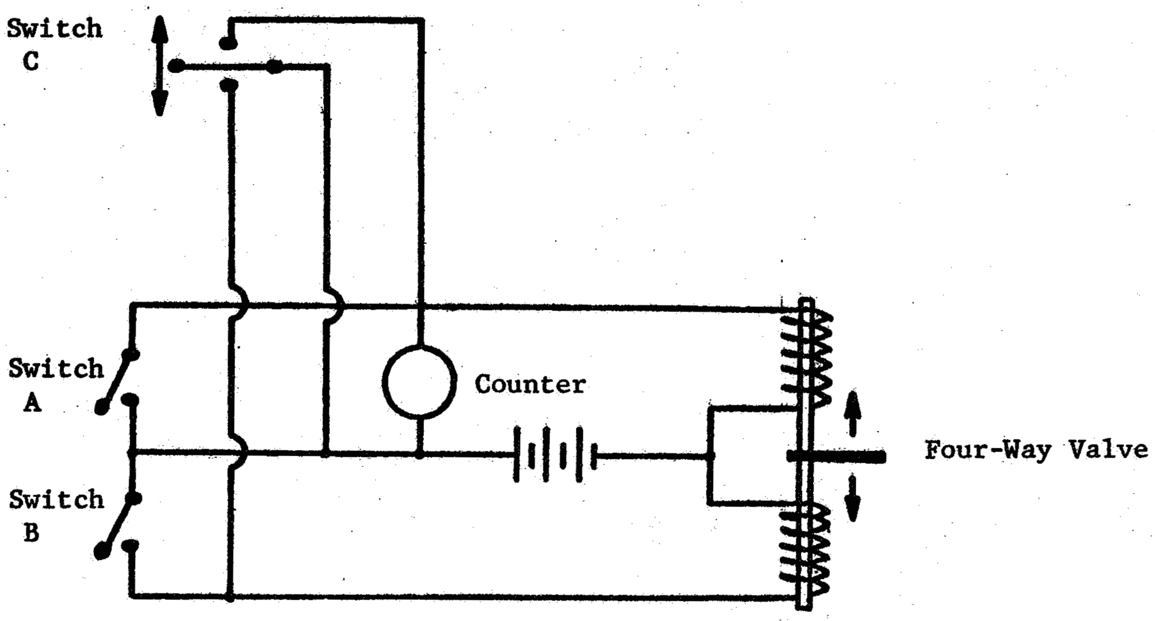

Figure C-8. Schematic Diagram of the Electric Solenoid-Circuit

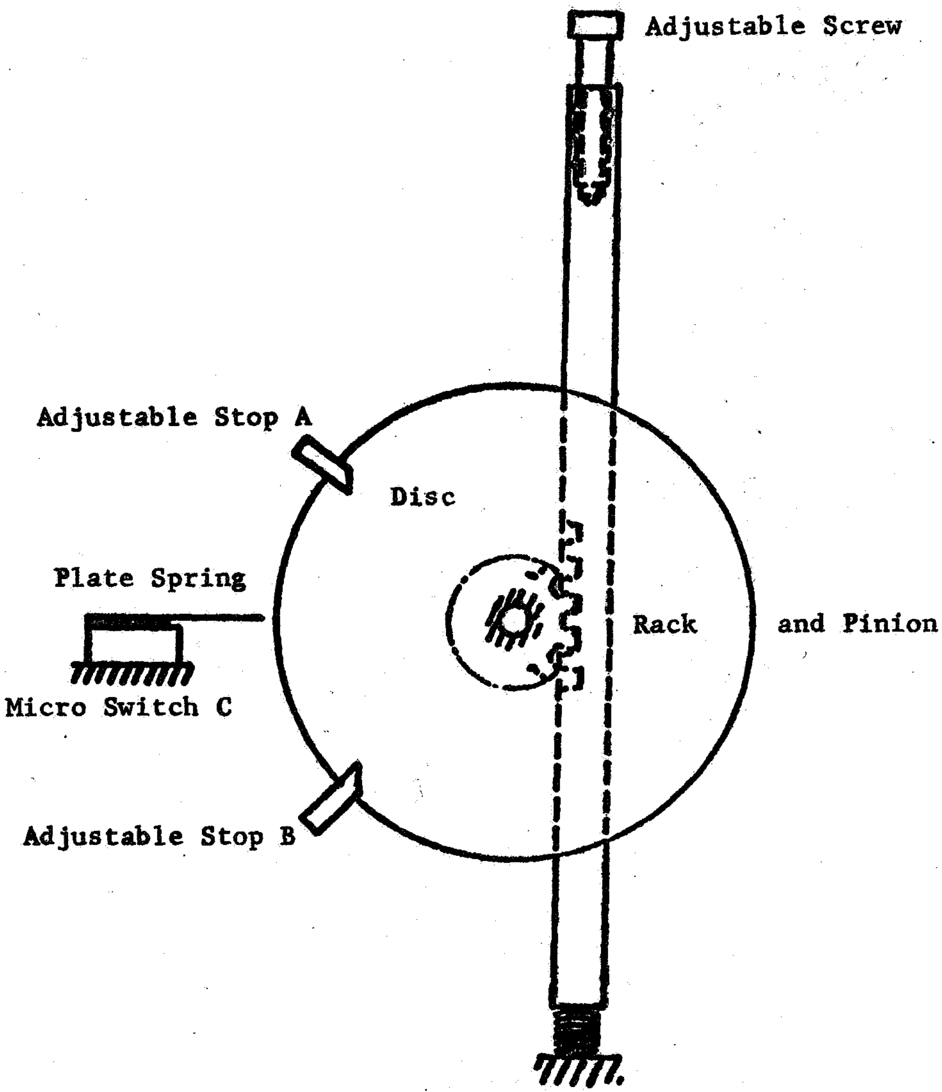

Figure C-9. Deflection Monitor

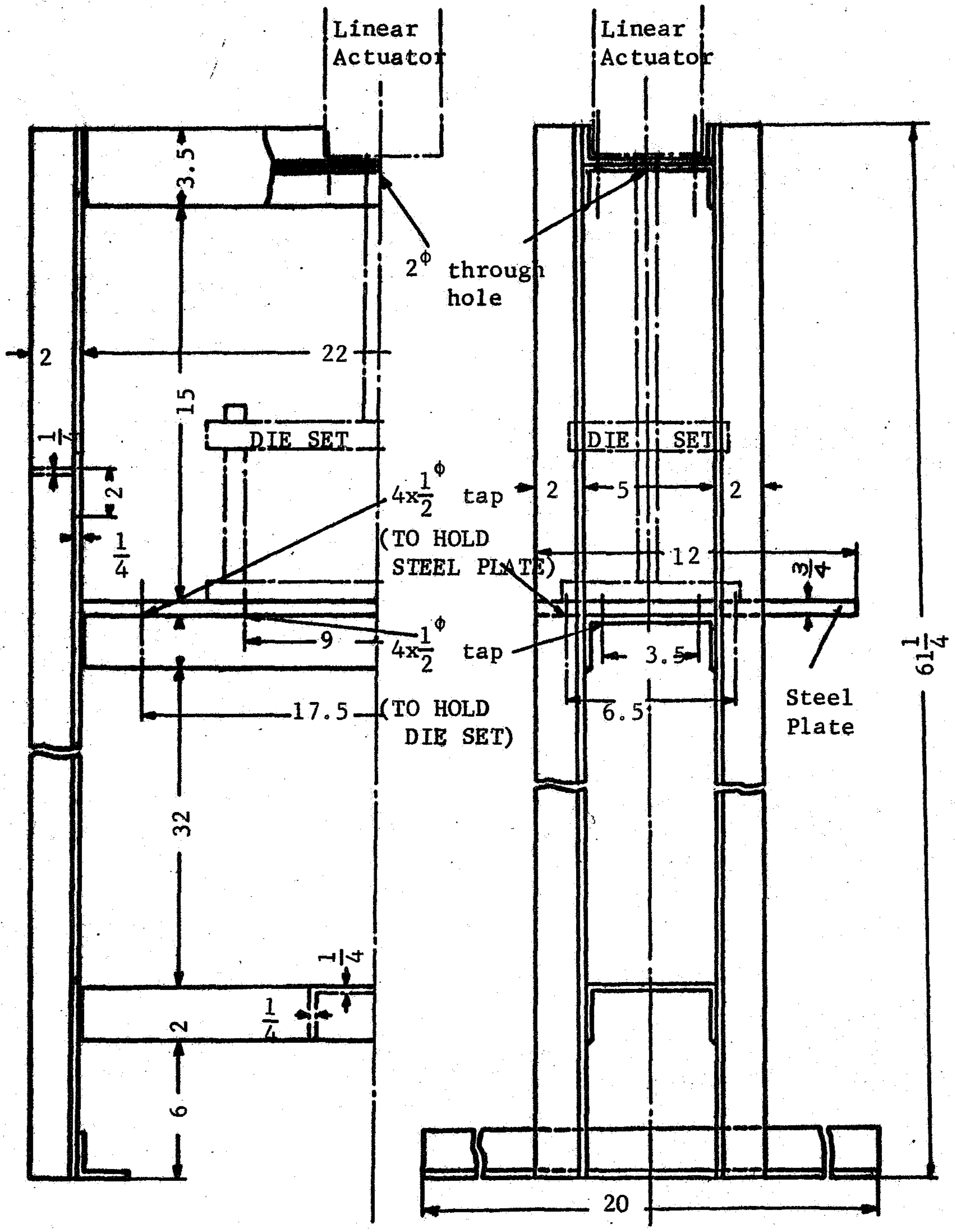

Figure C-10. Frame